Master's thesis

NTNU
Norwegian University of Science and Technology
Faculty of Engineering
Department of Civil and Environmental Engineering

Knut Reidulff

Wave environment assessment at a Norwegian harbor for land-based aquaculture facilities using a combined numerical approach

Master's thesis in Civil and Environmental Engineering
Supervisor: Hans Bihs
Co-supervisor: Weizhi Wang
June 2021

NTNU
Kunnskap for en bedre verden

Knut Reidulff

Wave environment assessment at a Norwegian harbor for land-based aquaculture facilities using a combined numerical approach

Master's thesis in Civil and Environmental Engineering
Supervisor: Hans Bihs
Co-supervisor: Weizhi Wang
June 2021

Norwegian University of Science and Technology
Faculty of Engineering
Department of Civil and Environmental Engineering

NTNU
Norwegian University of
Science and Technology

Abstract

Numerical wave modeling of Norwegian coastal areas is challenging due to the strongly varying bathymetry, irregular coastline, and large domains of interest. Phase-averaged models provide an appealing solution due to their computational efficiency, but have limitations in areas of strongly varying bathymetry and irregular coastline. Phase-resolved models provide higher accuracy with the trade-off of significantly higher computational cost. The goal of the study is to provide an open-source combined modeling approach to harbor design and use the approach to analyze the the wave conditions at two proposed locations for on-shore aquaculture facilities at Fiskenes and Breivik, Andøya.

The numerical wave models chosen for this thesis is the phase-averaged model SWAN and the phase-resolved model REEF3D::FNPF. The analysis will be performed in three model steps, with increasing accuracy closer to the proposed locations of Fiskenes and Breivik. The phase-averaged analysis in SWAN will employ a nested approach between simulation steps, and an interpolation scheme is used to obtain more information about possible met-ocean conditions without requiring additional simulations. A unidirectional spectrum extracted from the SWAN simulation will serve as the input for the REEF3D::FNPF simulation.

Analysis of wave conditions at Fiskenes and Breivik show that there is strong wave transformation at both locations, but due to stronger diffraction from northerly waves at Breivik, the waves are smaller at this location. At two possible locations of the breakwaters, the a significant wave height is estimated to be 2.90 meters for Fiskenes and 1.74 meters for Breivik.

The thesis concludes that the combined numerical modeling approach using SWAN and REEF3D::FNPF is an effective solution for coastal wave modeling in Norwegian conditions. REEF3D::FNPF has also shown to be a powerful phase-resolved model for near-shore analysis capturing wave transformations such as shoaling, diffraction, and energy dissipation from breaking well.

Acknowledgments

After four years in Trondheim and one year in Maryland, USA, I am finally done as a graduate student at NTNU. I would like to thank the consulting firm, for supplying me with the data for the analysis and for showing continued interest in my work. I am also grateful for my supervisor, Associate Professor Hans Bihs, who made this thesis possible and has taught me most of what I know in the field of numerical wave modeling.

A special thanks to my co-supervisor, Postdoctoral Fellow Weizhi Wang, for his interest in my thesis and for always being available for discussions. His support and expertise in numerical wave modeling has been truly invaluable.

I'd also like to thank my family for their continued support and for giving me every opportunity to succeed in life.

Finally, an acknowledgement to my roommates and childhood friends, Martin Amaral Halseide, Torstein Mellingen Langan, and Håvard Katle Fjon, thank you for five years of great memories.

Contents

List of Figures

Chapter 1

Introduction

1.1 Background

Land-based fish farming has roots back in the 60s but has never been a commercially viable option compared to its net-based counterpart at sea (Fjørtoft and Fondevik [2020]). Technological progresses, however, such as developments in recirculating aquaculture systems (RAS), have created profitable opportunities for land-based fish farming (Fjørtoft and Fondevik [2020]). In addition to the technical readiness, the concern over environmental impacts from the water-born net-based fish farms has also made the land-based alternative more attractive. A newly established company, has obtained a concession from the Norwegian government to produce 10 000 metric tonnes of farmed salmon at Andøya (Andfjord Salmon [2021]). The company also owns land rights for further expansion to additional locations at Andøya including Fiskenes, Breivik, and Kvalnes, as seen in Fig. 1.1.

Andøya is located in the Norwegian archipelago Lofoten - Vesterålen and has unique advantages for Atlantic salmon farming. The inflow of continuous oxygen-rich seawater from the Gulf stream, see Fig. 1.1, provides stable sea-water temperatures which are excellent for salmon growth and health in the shore-based tanks. Although the facility will be based onshore, construction of a breakwater is necessary to protect the farming facility in addition to providing shelter and safe harboring for ships docking to provide feed for the salmon.

Although Andøya has several advantages for farming salmon, its coastal area is subject to strong wind and severe wave conditions. In addition, the drastically changing bathymetry and irregular coastline make wave modeling a challenging endeavor. A consulting firm has completed an analysis of wave conditions of the proposed locations of Fiskenes and Breivik harbor for offshore swell waves in addition to a fetch

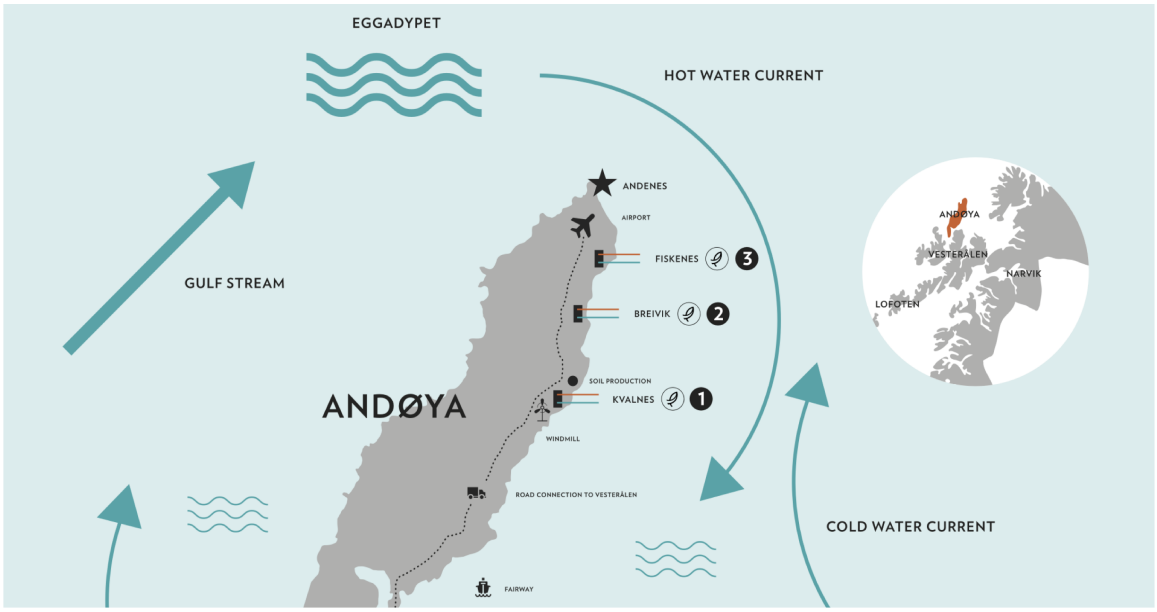

Figure 1.1: Possible fish farming locations and overview of Andøya.
source: Andfjord Salmon [2021]

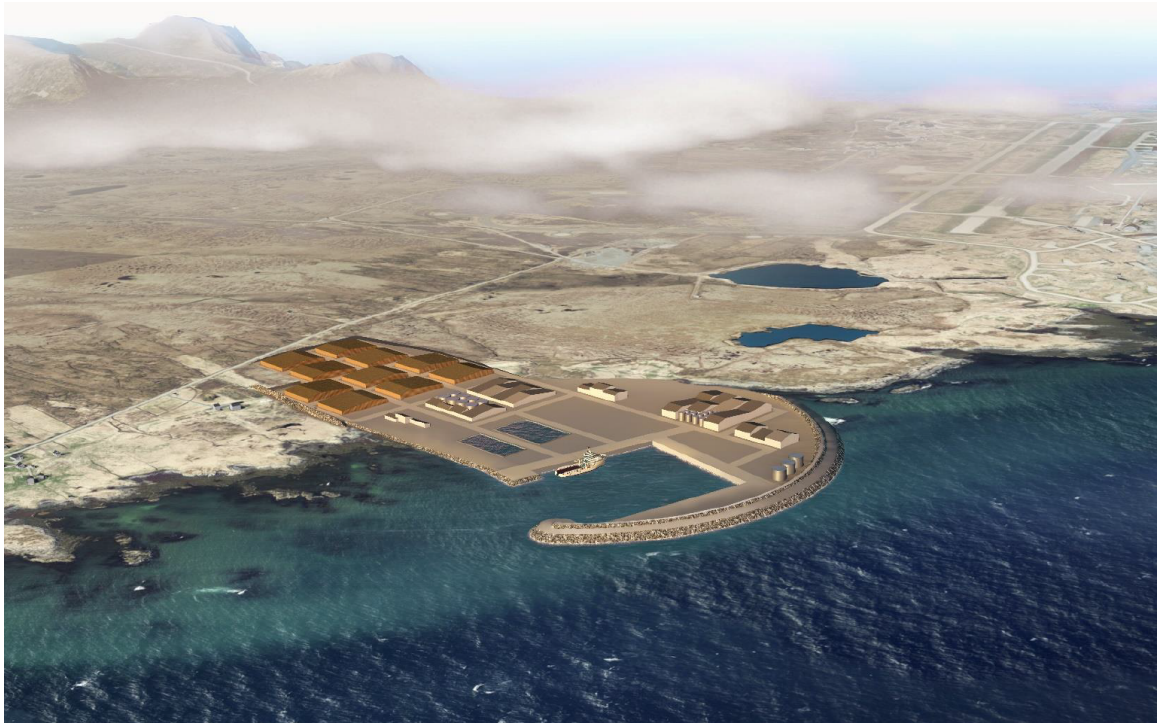

Figure 1.2: Fiskenes Harbor concept, generated by the consulting firm

analysis for wind-generated waves. This thesis will evaluate the former, using a combination of the spectral model SWAN and the fully non-linear potential flow model REEF3D::FNPF to evaluate extreme values for offshore waves for breakwater construction at the two locations.

1.2 State-of-the-Art

1.2.1 Numerical Wave Models

Phase-averaging models, such as spectral models, are the most common wave model used by consulting firms today. Some of the most widely used spectral wave models are summarized in Table 1.1. Spectral models such as SWAN and STWAVE are two-dimensional and use a multi-directional wave spectrum to represent the wave state in the simulated domain (Ardhuin and Roland [2013]). Although the phase-averaging approach to wave modeling is very computationally efficient, they do not provide information about local maxima (Ardhuin and Roland [2013]). For some locations, such as the coastal areas of western Europe, and in deep and intermediate waters with small variations in bathymetry, spectral models such as SWAN and STWAVE have proven to provide reliable results. In addition, it is significantly easier to add the influence from winds and currents into a simulation as source terms in the governing equation of a spectral wave model. Regardless of the computational efficiency and the ability to easily include the effects from wind and currents, spectral models have an inherent weakness in coastal areas with strongly varying bathymetry and irregular coastlines (Wang [2020]). Norway's coast is known for its large variations in bathymetry, islands, and jagged coastline making spectral models such as SWAN less suitable. The use of spectral models at inappropriate locations may lead to incorrect estimations of the sea-state and thus incorrect design basis for coastal structures.

Another wave model is therefore needed to ensure sufficient accuracy in the wave modeling results for coastal regions in Norway. Phase-resolving models provide an attractive alternative to the commonly used phase-averaging models. Unlike phase-averaging spectral models, phase-resolving models explicitly reproduce the free surface and the velocity field. Reproducing the free surface and velocity field enables phase-resolving models to capture the quick variations in wave parameters and bathymetry in addition to produce reasonable estimates for local extreme values (Wang [2020]). The downside of phase-resolving models, however, is that the increased accuracy comes with an associated high computational cost, often several orders of magnitude higher than spectral models, usually requiring high-performance computing (HPC) facilities to conduct an analysis in a reasonable time.

Phase-averaging wave model	Technique
SWAN	Wave action balance
WAM	Wave action balance
MIKE SW	Wave action balance
STWAVE	Wave action balance

Table 1.1: Overview of some common phase-averaging wave models

Phase-resolving wave model	Model type	Technique
MIKE BW	SWE	Boussinesq
FUNWAVE	SWE	Boussinesq
REEF3D::SFLOW	SWE	Non-hydrostatic
SWASH	NH	Non-hydrostatic
CGWAVE	EMSE	Elliptic Mild-slope Equation
SPHysics	SPH	Smooth-particle Hydrodynamics
HOS-NWT	Potential flow	High-order Spectrum
Whisper3D	Potential flow	High-order Spectrum
OceanWave3D	Potential flow	Finite Difference Method
REEF3D::FNPF	Potential flow	Finite Difference Method
OpenFOAM	CFD	Volume of Fluids
ANSYS-Fluent	CFD	Volume of Fluids
Star CCM+	CFD	Volume of Fluids
REEF3D::CFD	CFD	Level-set Method

Table 1.2: Overview of some common phase-resolving wave models

In the scope of phase-resolving wave models, there are several different models based on different governing equations and with varying degrees of complexity. The most exact phase-resolving models are solving the Navier Stokes' equations (NSE), such as direct numerical simulation (DNS), large eddy simulation (LES), and Reynolds-averaged Navier-Stokes equations (RANS). Although the aforementioned models are accurate, a significant amount of computational resources and time is required to run simulations, even when using HPC facilities. Their computational demands make them less viable for wave modeling in large domains of interest, which is often required for coastal wave modeling. There are several phase-resolving models with more moderate demand on computational resources when using available HPC facilities and workstations. Such models include Boussinesq wave models, two-dimensional shallow-water wave models (SWE), and fully non-linear potential flow models (FNPF). An overview of both open-source and commercial wave modeling software is outlined in Table 1.2.

As discussed, there are several wave modeling options with their own inherent advantages and disadvantages. In the ideal case, one would use phase-averaging models in areas where they are sufficiently accurate, and a phase resolving model only in the areas where the capabilities of phase-averaging models is surpassed. In a practical case, this would be for example using a phase-averaging spectral model for the large-scale modeling of offshore waves until an area quite near a harbor, a phase-resolved Boussinesq model for the near-shore simulation, and a RANS CFD model for estimating forces on the harbor structure. This way, high resolution flow field information can be captured while maintaining high computational efficiency.

The combined use of spectral wave models and phase-resolving models have been performed by the academy and industry for the combined advantages of both modelling approaches. In the consulting firms' approach, two commercial wave models were used, the phase-averaging spectral model STWAVE and the phase-resolving shallow water wave model CGWAVE. In this study, two open-source wave models is used in conjunction, similar to the consulting firms' case. For the large-scale simulation, the phase-averaging open-source model SWAN will be used, and for the nearshore simulation, the phase-resolving fully non-linear potential flow model REEF3D::FNPF will is used.

1.3 Objectives of the study

The goal of the study is to provide an open-source combined modeling approach to coastal wave modeling and use the approach to analyze the the wave conditions at the Fiskenes and Breivik. Specifically, the objectives of the study is the following:

- Design a nested approach for the spectral wave modelling of the offshore wave environment with varying input wave conditions and directions.
- Configure a phase-resolving numerical wave tank for the adjacent area of the candidate harbors.
- Combine the two wave models and the varying wave conditions to provide an overview of the coastal wave conditions due to offshore swell near Fiskenes and Breivik with different scenarios.

Chapter 2

Numerical Model - REEF3D::FNPF

Chapter 2 will briefly discusses the basic concepts of fully non-linear potential flow (FNPF) and the computational methods employed by REEF3D (Bihs et al. [2016], Alagan Chella et al. [2019], Ahmad et al. [2020], Martin et al. [2020]). The review of the model numerical model is conducted with reference to Wang [2020].

2.1 Governing Equation

The governing equation for the flow calculations in the open-source fully non-linear potential flow code REEF3D::FNPF (Bihs et al. [2020], Wang et al. [2019]) is the Laplace equation:

$$\frac{\partial^2 \Phi}{\partial x^2} + \frac{\partial^2 \Phi}{\partial y^2} + \frac{\partial^2 \Phi}{\partial z^2} = 0 \tag{2.1}$$

In order to solve for the velocity potential Φ, this elliptic equation requires boundary conditions, where especially the ones at the free surface and the bed are of importance. At the free surface, the fluid particles should remain at the surface and the pressure in the fluid is equal to the atmospheric pressure. These conditions must hold true at the free surface at all times and they form the kinematic and dynamic boundary conditions at the free surface respectively:

$$\frac{\partial \eta}{\partial t} = -\frac{\partial \eta}{\partial x}\frac{\partial \widetilde{\phi}}{\partial x} - \frac{\partial \eta}{\partial y}\frac{\partial \widetilde{\phi}}{\partial y} + \widetilde{w}\left(1 + \left(\frac{\partial \eta}{\partial x}\right)^2 + \left(\frac{\partial \eta}{\partial y}\right)^2\right) \tag{2.2}$$

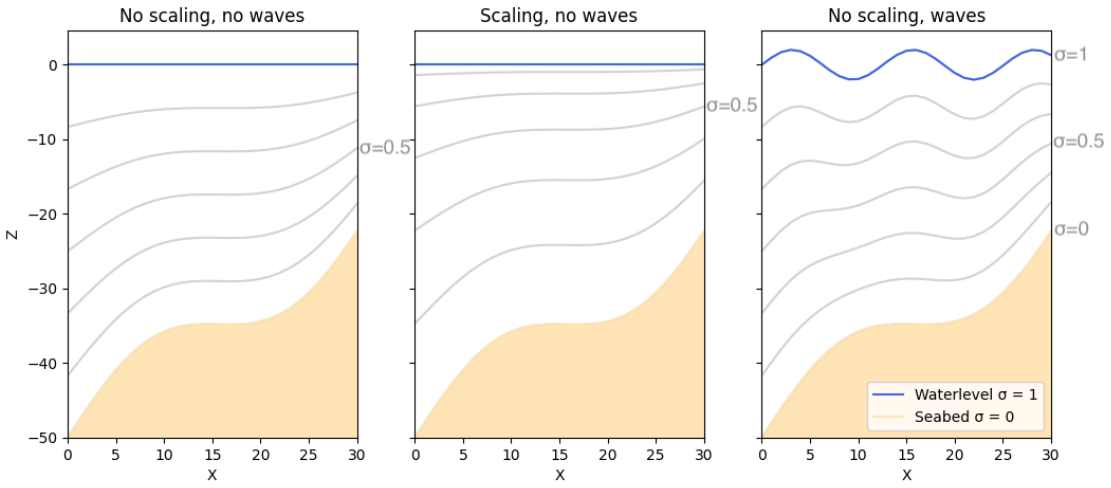

Figure 2.1: 2D σ-grid over varying bathymetry and waves

$$\frac{\partial \widetilde{\phi}}{\partial t} = -\frac{1}{2}\left(\left(\frac{\partial \widetilde{\phi}}{\partial x}\right)^2 + \left(\frac{\partial \widetilde{\phi}}{\partial y}\right)^2 - \widetilde{w}^2\left(1 + \left(\frac{\partial \eta}{\partial x}\right)^2 + \left(\frac{\partial \eta}{\partial y}\right)^2\right)\right) - g\eta \tag{2.3}$$

where η is the free surface elevation, $\widetilde{\phi} = \phi(\mathbf{x}, \eta, t)$ is the velocity potential at the free surface. $\mathbf{x} = (x, y)$ is the location in the x-y plane and $\widetilde{\omega}$ is the vertical velocity at the free surface.

The boundary condition at the bottom, where $z = -h$, vertical particle velocity must be zero since the particle cannot penetrate the bottom boundary. Where the bottom bathymetry is not flat, the velocity component normal to the bottom surface must be zero. Thus we get the generalized boundary condition:

$$\frac{\partial \Phi}{\partial z} + \frac{\partial h}{\partial x}\frac{\partial \Phi}{\partial x} + \frac{\partial h}{\partial y}\frac{\partial \Phi}{\partial y} = 0, \quad z = -h. \tag{2.4}$$

where $h = h(\mathbf{x})$ is the water depth measured from still water level at $\mathbf{x} = (x, y)$ in the x-y plane.

In REEF3D::FNPF, the Laplace equation and boundary conditions are solved in a σ-coordinate system. The σ-coordinate system follows the bathymetry and the free surface such that with decreasing water depth, the vertical spacing of the grid decrease, as illustrated in Fig. 2.1. In the model, the vertical coordinates follow the form of a Cartesian coordinate system, the σ-grid is defined as follows:

$$\sigma = \frac{z + h\left(\mathbf{x}\right)}{\eta(\mathbf{x}, t) + h(\mathbf{x})} \tag{2.5}$$

Near the surface, a more refined mesh is required to ensure sufficient accuracy. In the model, the vertical coordinates are defined from the following stretching function such that the grid becomes denser toward the free-surface:

$$\sigma_i = \frac{\sinh(-\alpha) - \sinh\left(\alpha\left(\frac{i}{N_z} - 1\right)\right)}{\sinh(-\alpha)} \tag{2.6}$$

The velocity potential ϕ after the σ-grid transformation is denoted as Φ. The boundary conditions are the same as for a Cartesian coordinate system, but with the free surface at $\sigma = 1$ and the bottom at $\sigma = 0$.

$$\begin{array}{ll} \Phi = \widetilde{\phi} & ,\sigma = 1 \\ \frac{\partial^2\Phi}{\partial x^2} + \frac{\partial^2\Phi}{\partial y^2} + \left(\frac{\partial^2\sigma}{\partial x^2} + \frac{\partial^2\sigma}{\partial y^2}\right)\frac{\partial\Phi}{\partial\sigma} + 2\left(\frac{\partial\sigma}{\partial x}\frac{\partial}{\partial x}\left(\frac{\partial\Phi}{\partial\sigma}\right) + \right. & \\ \left.\frac{\partial\sigma}{\partial y}\frac{\partial}{\partial y}\left(\frac{\partial\Phi}{\partial\sigma}\right) + \left(\left(\frac{\partial\sigma}{\partial x}\right)^2 + \left(\frac{\partial\sigma}{\partial y}\right)^2 + \left(\frac{\partial\sigma}{\partial z}\right)^2\right)\frac{\partial^2\Phi}{\partial\sigma^2} = 0\right. & ,0 \leq \sigma < 1; \\ \left(\frac{\partial\sigma}{\partial z} + \frac{\partial h}{\partial x}\frac{\partial\sigma}{\partial x} + \frac{\partial h}{\partial y}\frac{\partial\sigma}{\partial y}\right)\frac{\partial\Phi}{\partial\sigma} + \frac{\partial h}{\partial x}\frac{\partial\Phi}{\partial x} + \frac{\partial h}{\partial y}\frac{\partial\Phi}{\partial y} = 0 & ,\sigma = 0 \end{array} \tag{2.7}$$

After the velocity potential Φ is solved in the σ-grid one may solve for the velocities:

$$u\left(\mathbf{x}, z\right) = \frac{\partial\Phi\left(\mathbf{x}, z\right)}{\partial x} = \frac{\partial\Phi\left(\mathbf{x}, \sigma\right)}{\partial x} + \frac{\partial\sigma}{\partial x}\frac{\partial\Phi\left(\mathbf{x}, \sigma\right)}{\partial\sigma}, \tag{2.8}$$

$$v\left(\mathbf{x}, z\right) = \frac{\partial\Phi\left(\mathbf{x}, z\right)}{\partial y} = \frac{\partial\Phi\left(\mathbf{x}, \sigma\right)}{\partial y} + \frac{\partial\sigma}{\partial y}\frac{\partial\Phi\left(\mathbf{x}, \sigma\right)}{\partial\sigma}, \tag{2.9}$$

$$w\left(\mathbf{x}, z\right) = \frac{\partial\sigma}{\partial z}\frac{\partial\Phi\left(\mathbf{x}, \sigma\right)}{\partial\sigma}. \tag{2.10}$$

2.2 Numerical schemes

The solution of the governing equation is performed in a discretized and iterative manner. In the 3D case, which is what is relevant for this study, a set number of points on the 3D grid is defined. The process of defining discrete points over a domain for numerical simulation is called spatial discretization.

The discretization of the gradient terms of the free-surface boundary conditions, eq. 2.7, is conducted with the use of the 5th-order Hamilton Jacobi version of the weighted essentially non-oscillatory (WENO) scheme Jiang and Shu [1996]. The WENO stencil has three essentially non-oscillatory (ENO) stencils based on smoothness indicators IS (Jiang and Shu [1996]). The scheme is designed in such a manner that the local

stencil with the lowest IS (the highest smoothness) gets assigned the largest weight ω_i. This ensures that the stencils with the highest smoothness contributes the most to gradient term and thus enables the scheme to handle large gradients with good accuracy. The WENO approximation of Φ is a linear combination the three possible ENO approximations. In the x-direction, the discretization is formulated as following: Weighted Essentially Non- Oscillatory (WENO) Scheme

$$\phi_x = \begin{cases} \phi_x^- & if\ U_1 > 0 \\ \phi_x^+ & if\ U_1 < 0 \\ 0 & if\ U_1 = 0 \end{cases} \tag{2.11}$$

The WENO approximation for $\phi_x^{\pm}$ is a convex combination of the three possible ENO approximations:

$$\phi_x^{\pm} = \omega_1^{\pm}\phi_x^{1\pm} + \omega_2^{\pm}\phi_x^{2\pm} + \omega_3^{\pm}\phi_x^{3\pm} \tag{2.12}$$

The three ENO stencils defined for ϕ are

$$\begin{aligned} \phi_x^{1\pm} &= \frac{q_1^{\pm}}{3} - \frac{7q_2^{\pm}}{6} + \frac{11q_3^{\pm}}{6} \\ \phi_x^{2\pm} &= -\frac{q_2^{\pm}}{6} + \frac{5q_3^{\pm}}{6} + \frac{q_4^{\pm}}{3} \\ \phi_x^{3\pm} &= \frac{q_3^{\pm}}{3} + \frac{5q_4^{\pm}}{6} - \frac{q_5^{\pm}}{6} \end{aligned} \tag{2.13}$$

with,

$$\begin{aligned} q_1^- &= \frac{\phi_{i-2} - \phi_{i-3}}{\Delta x},\ q_2^- = \frac{\phi_{i-1} - \phi_{i-2}}{\Delta x},\ q_3^- = \frac{\phi_i - \phi_{i-1}}{\Delta x}, \\ q_4^- &= \frac{\phi_{i+1} - \phi_i}{\Delta x},\ q_5^- = \frac{\phi_{i+2} - \phi_{i+1}}{\Delta x} \end{aligned} \tag{2.14}$$

and

$$\begin{aligned} q_1^+ &= \frac{\phi_{i+3} - \phi_{i+2}}{\Delta x},\ q_2^+ = \frac{\phi_{i+2} - \phi_{i+1}}{\Delta x},\ q_3^+ = \frac{\phi_{i+1} - \phi_i}{\Delta x}, \\ q_4^+ &= \frac{\phi_i - \phi_{i-1}}{\Delta x},\ q_5^+ = \frac{\phi_{i-1} - \phi_{i-2}}{\Delta x} \end{aligned} \tag{2.15}$$

the weights are written as:

$$\omega_1^{\pm} = \frac{\alpha_1^{\pm}}{\alpha_1^{\pm} + \alpha_2^{\pm} + \alpha_3^{\pm}},\ \ \omega_2^{\pm} = \frac{\alpha_2^{\pm}}{\alpha_1^{\pm} + \alpha_2^{\pm} + \alpha_3^{\pm}},\ \ \omega_3^{\pm} = \frac{\alpha_3^{\pm}}{\alpha_1^{\pm} + \alpha_2^{\pm} + \alpha_3^{\pm}}, \tag{2.16}$$

and

$$\alpha_1^{\pm} = \frac{1}{10}\frac{1}{\left(\widetilde{\epsilon} + IS_1^{\pm}\right)^2}, \quad \alpha_2^{\pm} = \frac{6}{10}\frac{1}{\left(\widetilde{\epsilon} + IS_2^{\pm}\right)^2}, \quad \alpha_3^{\pm} = \frac{3}{10}\frac{1}{\left(\widetilde{\epsilon} + IS_3^{\pm}\right)^2} \tag{2.17}$$

with the regularization parameter $\widetilde{\epsilon} = 10^{-6}$ in order to avoid division by zero and the following smoothness indicators:

$$\begin{aligned} IS_1^{\pm} &= \frac{13}{12}\left(q_1 - 2q_2 + q_3\right)^2 + \frac{1}{4}\left(q_1 - 4q_2 + 3q_3\right)^2, \\ IS_2^{\pm} &= \frac{13}{12}\left(q_2 - 2q_3 + q_4\right)^2 + \frac{1}{4}\left(q_2 - q_4\right)^2, \\ IS_3^{\pm} &= \frac{13}{12}\left(q_3 - 2q_4 + q_5\right)^2 + \frac{1}{4}\left(3q_3 - 4q_4 + q_5\right)^2 \end{aligned} \tag{2.18}$$

2.2.1 Time Discretization

The time treatment is based on a 3rd-order accurate total variation diminishing (TVD) Runge-Kutta scheme Shu and Osher [1988].

$$\begin{aligned} \phi^{(1)} &= \phi^n + \Delta t L\left(\phi^n\right) \\ \phi^{(2)} &= \frac{3}{4}\phi^n + \frac{1}{4}\phi^{(1)} + \frac{1}{4}\Delta t L\left(\phi^{(1)}\right) \\ \phi^{n+1} &= \frac{1}{3}\phi^n + \frac{2}{3}\phi^{(2)} + \frac{2}{3}\Delta t L\left(\phi^{(2)}\right) \end{aligned} \tag{2.19}$$

where L indicates the spatial discretization.

An example of its application is shown below.

$$\begin{aligned} \phi^{(1)} &= \phi^n + \frac{\Delta t}{2} L\left(\phi^n\right) \\ \phi^{(2)} &= \phi^n + \frac{\Delta t}{2} L\left(\phi^{(1)}\right) \\ \phi^{(3)} &= \phi^n + \Delta t L\left(\phi^{(2)}\right) \\ \phi^{n+1} &= \frac{-1}{3}\phi^n + \frac{1}{3}\phi^{(1)} + \frac{2}{3}\phi^{(2)} + \frac{1}{3}\phi^{(3)} + \frac{\Delta t}{6} L\left(\phi^{(3)}\right) \end{aligned} \tag{2.20}$$

2.2.2 Adaptive Time Stepping

Adaptive time stepping is not necessary, but for increased accuracy and efficiency of the solver, adaptive time stepping is implemented with constant time factor is controlled with the Courant-Friedrichs-Lewy (CFL) condition:

$$
\begin{aligned}
c_u &= \frac{dx}{\left|\max\left(u_{\max}, 1.0\sqrt{9.81 * h_{\max}}\right)\right|} \\
c_v &= \frac{dx}{\left|\max\left(v_{\max}, 1.0\sqrt{9.81 * h_{\max}}\right)\right|} \\
c_{tot} &= \min\left(c_u, c_v\right) \\
dt &= c_{tot} CFL
\end{aligned}
\tag{2.21}
$$

where u_{max}, v_{max} are the maximum particle velocities in x and y directions at the free surface. h_{max} is the maximum water depth.

2.2.3 Laplace solver

For the simulations conducted in this study, the Laplace equation is discretized using second-order central differences using a parallelized geometric multigrid preconditioned conjugate gradient solver provided by Hypre van der Vorst [1992].

2.3 Wave generation and absorption

In REEF3D, the waves are generated using the relaxation method, where the wave generation takes place in a relaxation zone of approximately one wavelength.

In the relaxation zone, the velocities and the free surface is gradually increased from the computational values to the values obtained from wave theory 2.22. In addition to wave generation, waves propagating toward the inlet are absorbed with this method. At the outlet boundary of the domain, the waves need to be absorbed such that reflections will not influence results. In REEF3D, this is also achieved using the relaxation method. In the outlet relaxation zone, often referred to as the numerical beach, the velocities are reduced to zero in addition free surface and pressure reduced to the values for still water level. This ensures that the wave energy is absorbed and reflection of waves prevented.

$$
\begin{aligned}
u(\widetilde{x})_{\text{relaxed}} &= \Gamma(\widetilde{x}) u_{\text{analytical}} + (1 - \Gamma(\widetilde{x})) u_{\text{computational}} \\
w(\widetilde{x})_{\text{relaxed}} &= \Gamma(\widetilde{x}) w_{\text{analytical}} + (1 - \Gamma(\widetilde{x})) w_{\text{computational}} \\
p(\widetilde{x})_{\text{relaxed}} &= \Gamma(\widetilde{x}) p_{\text{analytical}} + (1 - \Gamma(\widetilde{x})) p_{\text{computational}} \\
\phi(\widetilde{x})_{\text{relaxed}} &= \Gamma(\widetilde{x}) \phi_{\text{analytical}} + (1 - \Gamma(\widetilde{x})) \phi_{\text{computational}}
\end{aligned}
\tag{2.22}
$$

In REEF3D, the relaxation function in Jacobsen et al. [2012] is used 2.23.

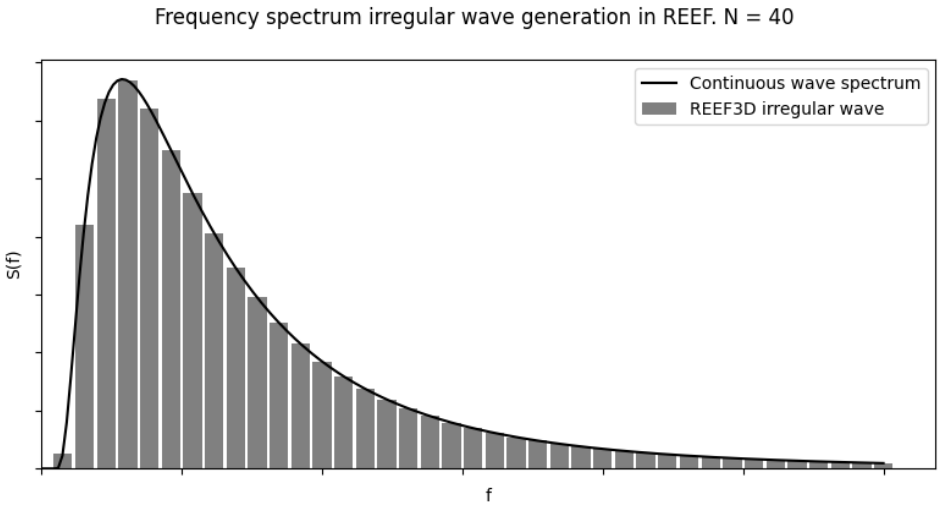

Figure 2.2: REEF3D irregular wave generation from spectrum

$$\Gamma(\widetilde{x}) = 1 - \frac{e^{\left(\widetilde{x}^{3.5}\right)} - 1}{e - 1} \text{ for } \widetilde{x} \in [0; 1] \tag{2.23}$$

The coordinate $\widetilde{x}$ is scaled to the length of the relaxation zone (one wavelength at inlet, two at outlet).

Irregular wave generation in REEF3D is quite simple, it follows the principle that all irregular waves are considered a summation of a finite number of regular waves. The wave spectrum describes the wave energy distribution over the given frequencies in the input of the domain. In the relaxation zone, REEF3D ramps up the hydrodynamic values prescribed by the wave spectrum. The number of regular waves $N_{regularwaves}$ used for in the irregular wave generation is selected by the user 2.2.

2.4 Breaking wave algorithm

REEF3D::FNPF represent the free surface by only a single value. An overturning wave needs to be represented with several values of the free surface and thus the model is unable to represent breaking waves such as in computational fluid dynamics (CFD) (Wang [2020]). Although overturning plunging breaking waves cannot be represented themselves, it is still important to include the energy dissipation that occurs with breaking waves. With an accurate breaking wave algorithm, accurate detection and dissipation may be simulated.

The breaking wave algorithm uses the depth-induced shallow water breaking criterion. The detection of a breaking wave occurs when the vertical velocity of the free surface exceed a fraction of the water celerity.

$$\frac{\partial \eta}{\partial t} \geq \alpha_s \sqrt{gh} \tag{2.24}$$

$\alpha_s = 0.6$ works well with most waves (Smit et al. [2013]).
Deepwater steepness-induced breaking is detected with the following steepness criterion:

$$\frac{\partial \eta}{\partial x_i} \geq \beta \tag{2.25}$$

After wave breaking is detected, the energy dissipation from the breaking wave process must be represented. There are two main methods for breaking wave energy dissipation, the geometric filtering algorithm Jensen et al. [1999] or by the introduction of a local viscous dampening term for the free-surface boundary condition around the breaking region Baquet et al. [2017]. A combination of the two methods may be used for complex breaking conditions for more accurate results. For the the viscous dampening method, the free surface boundary condition becomes:

$$\begin{aligned}
\frac{\partial \eta}{\partial t} =& -\frac{\partial \eta}{\partial x}\frac{\partial \widetilde{\phi}}{\partial x} - \frac{\partial \eta}{\partial y}\frac{\partial \widetilde{\phi}}{\partial y} + \widetilde{w}\left(1 + \left(\frac{\partial \eta}{\partial x}\right)^2 + \left(\frac{\partial \eta}{\partial y}\right)^2\right) \\
&+ \nu_b \left(\frac{\partial^2 \eta}{\partial x^2} + \frac{\partial^2 \eta}{\partial y^2}\right), \\
\frac{\partial \widetilde{\phi}}{\partial t} =& -\frac{1}{2}\left(\left(\frac{\partial \widetilde{\phi}}{\partial x}\right)^2 + \left(\frac{\partial \widetilde{\phi}}{\partial y}\right)^2 - \widetilde{w}^2\left(1 + \left(\frac{\partial \eta}{\partial x}\right)^2 + \left(\frac{\partial \eta}{\partial y}\right)^2\right)\right) \\
&- g\eta + \nu_b \left(\frac{\partial^2 \widetilde{\phi}}{\partial x^2} + \frac{\partial^2 \widetilde{\phi}}{\partial y^2}\right)
\end{aligned} \tag{2.26}$$

where v_b is the artificial turbulence viscosity. The v_b parameter has a recommended value of 1.86 for offshore deep-water wave conditions and 0.0055 for shallow-water waves Wang [2020]. v_b has been calibrated for FNPF with comparisons to model data and CFD simulations.

2.5 Coastline algorithm

Creating an efficient grid near the coastline whilst keeping numerical stability when applying a potential flow algorithm near the coastline is difficult. REEF3D::FNPF has its own coastline algorithm to address these issues.

The coastline algorithm firstly assigns all the cells in the domain as either wet or dry cells given the free surface elevation h being smaller or larger than a given value $\widehat{h}$. The default threshold $\widehat{h}$ is set to 0.0005 though it may be customized.

$$h = \eta + d \tag{2.27}$$

$$\begin{cases} u = 0, & \text{if } h < \widehat{h} \\ v = 0, & \text{if } h < \widehat{h} \end{cases} \tag{2.28}$$

After the identification, the wet and dry cells are assigned a value of +1 and -1 respectively, and the velocities in the cells are set to be zero. With the values assigned, the coastline is captured using a two-dimensional level-set function Osher and Sethian [1988]:

$$\phi(\vec{x}, t) \begin{cases} > 0 \text{ if } \vec{x} \in \text{ wet cell} \\ = 0 \text{ if } \vec{x} \in \Gamma \\ < 0 \text{ if } \vec{x} \in \text{ dry cell} \end{cases} \tag{2.29}$$

Γ indicates the coastline, and the Eikonal equation $|\nabla\phi| = 1$ holds true in the level-set function. The level-set method is also used to calculate the distance normal to the coastline. The signed distance property of the level-set function must be maintained to ensure mass conservation as the interfaces evolve.

Therefore, a reinitalization process is needed after every time step to calculate the distance to the coastline. REEF3D::FNPF uses a Partial Differential Equation (PDE) based reinitialization procedure Sussman [1994].

$$\frac{\partial \phi}{\partial \tau} + S(\phi)\left(\left|\frac{\partial \phi}{\partial x_j}\right| - 1\right) = 0 \tag{2.30}$$

where $S(\phi)$ is the smooth signed function.

$$S(\phi) = \frac{\phi}{\sqrt{\phi^2 + \left|\frac{\partial \phi}{\partial x_j}\right|^2 (\Delta x)^2}} \tag{2.31}$$

By using this level-set method, the computational grid remains the same with changes in topography. This gives the model great flexibility, as there is no need to generate a new grid for changes in the topography.

Along the wet side of the coastline, relaxation zones are applied. This ensures numerical stability and avoids extreme run-ups. In addition, the reflection of the coastline can be adjusted, which is of great importance when modelling close to

harbour areas where there is a varying degree of reflection from natural and artificial obstructions such as breakwaters.

Chapter 3

Numerical Model - SWAN

The spectral analysis is conducted in Simulating WAves Nearshore (SWAN) developed at TU Delft (SWAN [2020], Booij et al. [1999]). In this chapter, a short overview of the numerical methods employed in SWAN is discussed.

SWAN calculates the development of the sea state by the means of action density $N(\sigma, \theta)$. Action density is defined as the variance density $E(\sigma, \theta)$ divided by the relative frequency σ.

$$N(\sigma, \theta) = \frac{E(\sigma, \theta)}{\sigma} \tag{3.1}$$

where σ is the relative frequency and θ is the wave direction.

The evolution of the wave spectrum is described by an energy balance approach of the wave energy density. The balance of wave energy is defined in cells distributed in a two-dimensional grid. For all cells, of size $\delta x \delta y$, and over a time interval δt the following must be satisfied:

$$Change\ of\ energy = Net\ import\ of\ energy + Net\ local\ generation \tag{3.2}$$

By applying the principle of the energy balance approach we get the following expression for deep water in the absence of currents:

$$\frac{\partial}{\partial t}E + \frac{\partial}{\partial x}\left(c_x E\right) + \frac{\partial}{\partial y}\left(c_y E\right) = S(\sigma, \theta; x, y, t) \tag{3.3}$$

where c_x and c_y are components of the group velocity in the x and y direction, and $S(\sigma, \theta; x, y, t)$ is the source term that represents the effects of generation and dissipation.

If the energy balance equation, eq. 3.2, is applied to shallow water we obtain the following:

$$\frac{\partial}{\partial t}N + \frac{\partial}{\partial x}\left(\mathrm{c_x}N\right) + \frac{\partial}{\partial y}\left(c_y N\right) + \frac{\partial}{\partial \sigma}\left(c_\sigma N\right) + \frac{\partial}{\partial \theta}\left(c_\theta N\right) = \frac{S(\sigma,\theta;x,y,t)}{\sigma} \tag{3.4}$$

where,
$\frac{\partial}{\partial t}N$ - is the rate of change of action
$\frac{\partial}{\partial x}\left(\mathrm{c_x}N\right) + \frac{\partial}{\partial y}\left(c_y N\right)$ - represents the propagation of wave action in the 2D plane
$\frac{\partial}{\partial \sigma}\left(c_\sigma N\right)$ - represents the frequency shift
$\frac{\partial}{\partial \theta}\left(c_\theta N\right)$ - represents the refraction effects induced by currents and depth
$S(\sigma,\theta)$ - represents the effects from generation, dissipation and nonlinear wave-wave interactions.

In the SWAN model, $S(\sigma,\theta)$ is given by:

$$S(\sigma,\theta) = S_{inp}(\sigma,\theta) + S_{brk}(\sigma,\theta) + S_{frc}(\sigma,\theta) + S_{wcp}(\sigma,\theta) + S_{nl3}(\sigma,\theta) + S_{nl4}(\sigma,\theta) \tag{3.5}$$

where,
S_{inp} - generation due to wind input
S_{brk} - depth induced wave breaking
S_{frc} - bottom friction
S_{wcp} - whitecapping
S_{nl3} - triad wave-wave interactions
S_{nl4} - quadruplet wave-wave interactions

Chapter 4

Numerical verification

4.1 Varying bathymetry

To verify the accuracy of REEF3D::FNPF over varying bathymetry, a 2D submerged bar test is conducted with comparisons to experimental measurements Beji and Battjes [1993]. The benchmark test is a wave tank with a submerged bar reducing the depth gradually from 0.4 m to 0.1 m to initiate shoaling. Geometry of the numerical wave tank layout can be seen in Fig. 4.1, these values are identical to those in the real-world experiment Beji and Battjes [1993]. The properties of incident waves are outlined in Table 4.1.

The 2D experiment is achieved by the having the numerical wave tank be exactly one cell in the y-direction and defining the walls of the wave tank as symmetry planes.

Numerical wave gauges are placed in the same exact same locations as in the physical experiment such that a correct comparison can be made, see Fig. 4.1. The placement of the nodes ensure that we may capture all the wave effects from shoaling to the disrupted sea-state behind the bar. The results from the nine numerical wave gauges are presented in Fig. 4.2 and Fig. 4.3.

Wave gauge 1 is measuring waves directly after the wave generation zone and are therefore undisturbed, this gives confirmation that the incoming waves are identical to those in the experiment. At wave gauge 2 and 3, shoaling begins to occur due to

Wave length, L	Wave height, H	Cells x-dir	Cells z-dir	Δx
3.73 m	0.01 m	800	10	0.04375 m

Table 4.1: Relevant input parameters to numerical simulation

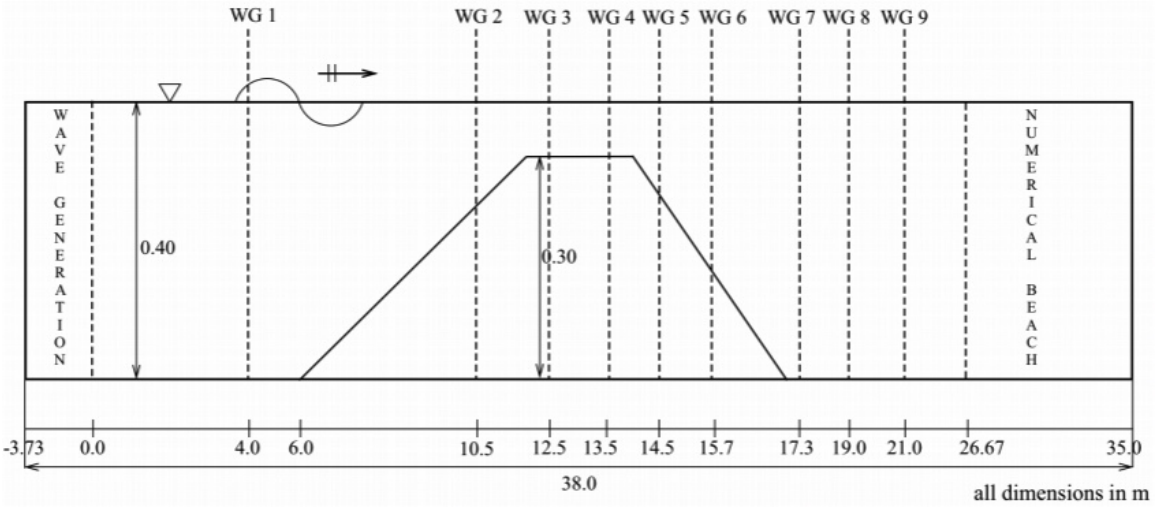

Figure 4.1: Dimensions of wave tank with submerged bar and location of wave gauges marked "WG"

the shallower water. The wave height increase to the point where the waves becomes unstable. It is evident that REEF3D has no difficulty with modelling the shoaling process. Also the decomposing of the waves is handled without any problems. The waves becomes too steep and the waves are decomposed into two (or more) wave components, which is visible at wave gauge 4 and 5. After the berm, the depth increases and the wave length increase along with a smaller wave height. At wave gauge 7, 8, and 9, there are minor deviations from the experiment and the REEF3D simulation in the most non-linear parts of the waves, see Fig. 4.3. Despite these small discrepancies, the numerical model are able to replicate both the form and size of the waves with good accuracy, as shown in Fig. 4.2 and Fig. 4.3.

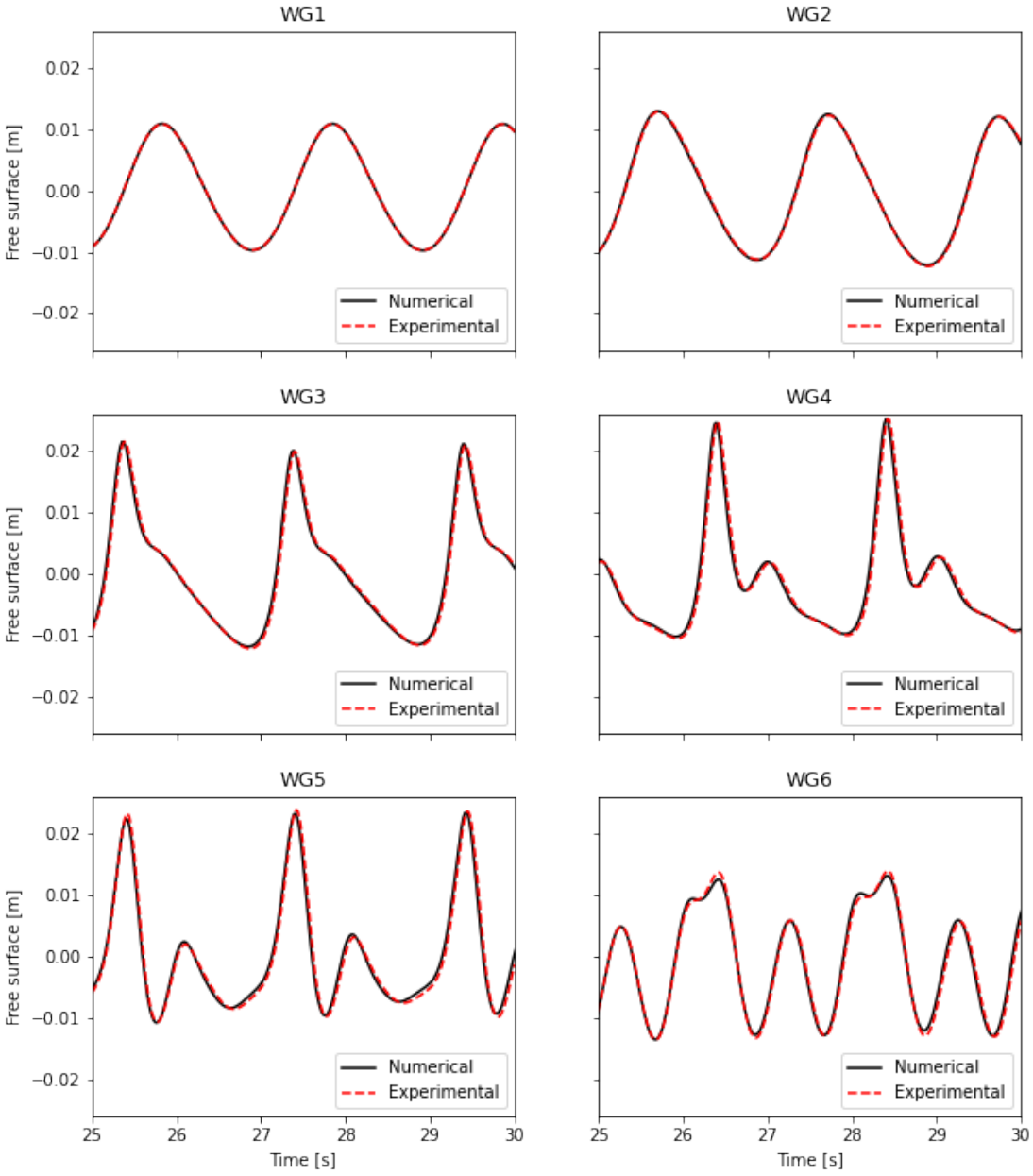

Figure 4.2: Free surface elevation at wave gauges 1-6

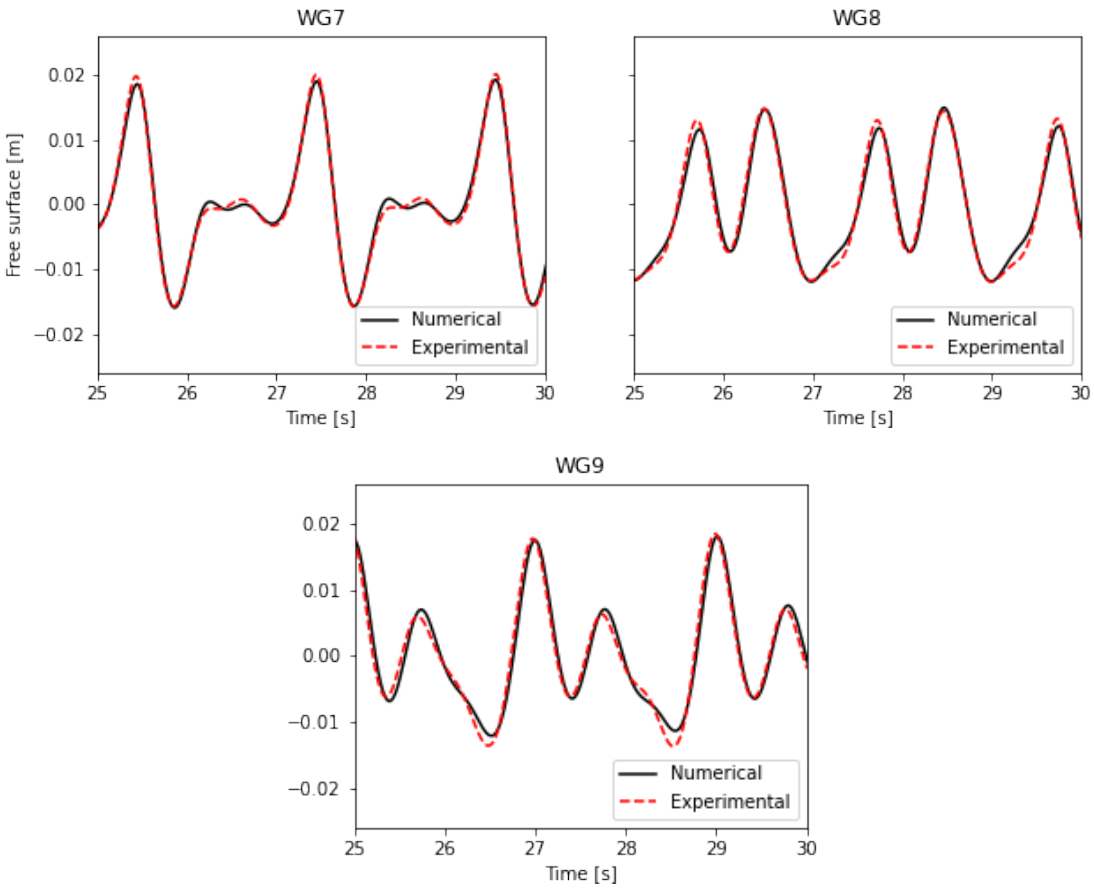

Figure 4.3: Free surface elevation at wave gauges 7-9

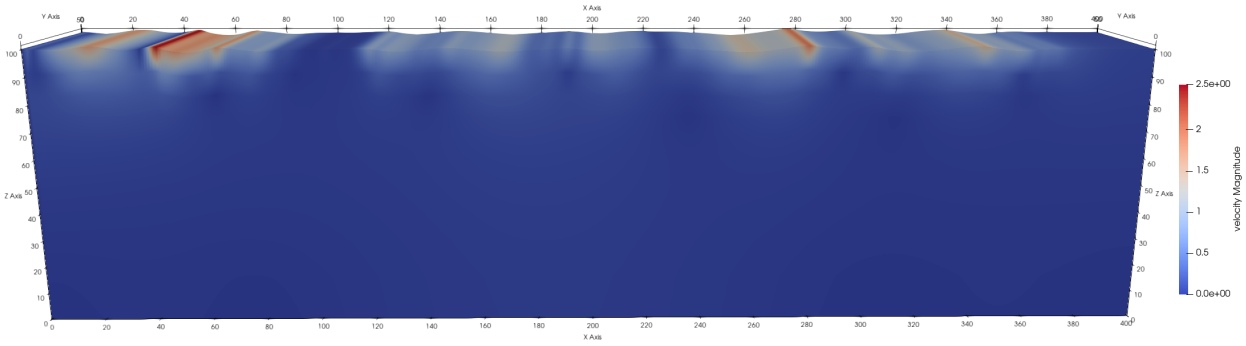

Figure 4.4: Numerical wave tank setup in REEF3D

X-extent	Y-extent	Z-extent	Cells x-dir	Cells y-dir	Cells z-dir
400 m	10 m	100 m	400	10	1

Table 4.2: Dimensions of the numerical wave tank and grid

4.2 Irregular wave generation

An output spectrum from SWAN has to be accurately replicated in REEF3D to ensure that the combined modeling approach may work. REEF3D has the capability to generate irregular waves from a unidirectional spectrum file. To ensure that REEF3D has the capability to generate waves from from the aforementioned spectrum file accurately, a two-dimensional wave tank was set up as seen in Fig. 4.4. The relevant parameters are outlined in Table 4.2. A common nearshore spectrum file was submitted and run for 10 000 seconds in order to generate a wave spectrum, see Fig. 4.5. The spectrum was generated from running an FFT analysis in Python, see Sec. 5.3.8, on a wave gauge placed directly after the wave generation zone.

Multiple tests cases were run with different cell sizes, it was shown that REEF3D was able to accurately generate waves corresponding to the input spectrum given that the wave generation zone was sufficiently long, approximately one wavelength. What was also discovered, was that for REEF3D::FNPF to simulate wave components with a higher frequency than 0.4 Hz, a 2.5 second wave period, the cell size may not be larger than 1m.

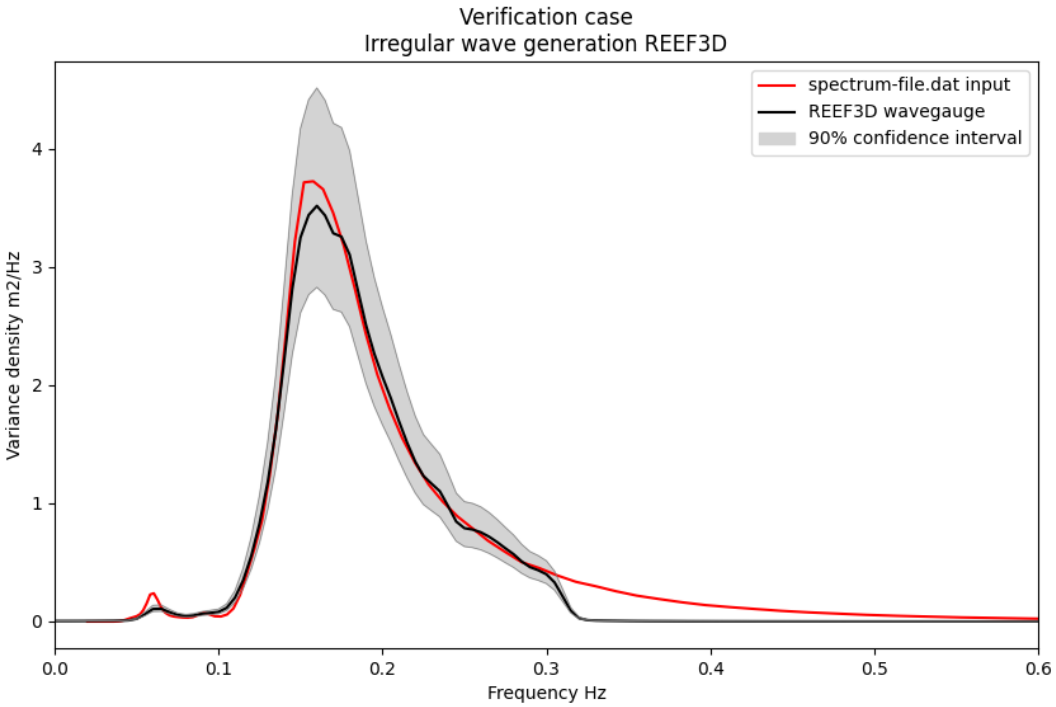

Figure 4.5: Output spectrum from verification case of irregular wave generation

Chapter 5

Method

The harbor was modeled in three main model steps. Due to the computational efficiency of spectral models and the desire to keep the comparisons with the consulting firm's approach close, the first two model steps were conducted in the open-source spectral model SWAN. The final simulation step will be computed in the phase-resolved model REEF3D::FNPF. The resulting wave-state for each simulation will be used as an input for the more refined simulation in the next model step.

5.1 Hindcast data

The offshore wave data was accessed using the WAM10 dataset Reistad et al. [2009]. The closest measuring point in the WAM10 data set is N70.73°/ E19.92°, about 200 kilometers NE of Andenes, see Fig. 5.3a. The WAM10 hindcast data is calculated using several measurements from 1957 to 2015 in order to predict extreme values for waves and wind. An overview of the return period for offshore waves can be seen in Fig. 5.1. According to the Norwegian regulations on technical requirements for construction works, TEK17 §7-2 (Norwegian Building Authority [2017]), the harbor and breakwater must be constructed to cope with a 200 year return period event. Therefore, this wave analysis is conducted with hindcast data for a 200 year return period, as summarized in Table 5.1.

5.2 SWAN Spectral modeling

Due to the phase-averaged approach of the spectral model SWAN being significantly more computationally efficient compared to the phase-resolving approach of REEF3D::FNPF, it was decided that the first two model steps were to be conducted in SWAN. The simulation will use a nested approach for transferring the wave conditions from simulations step 1 into simulation step 2.

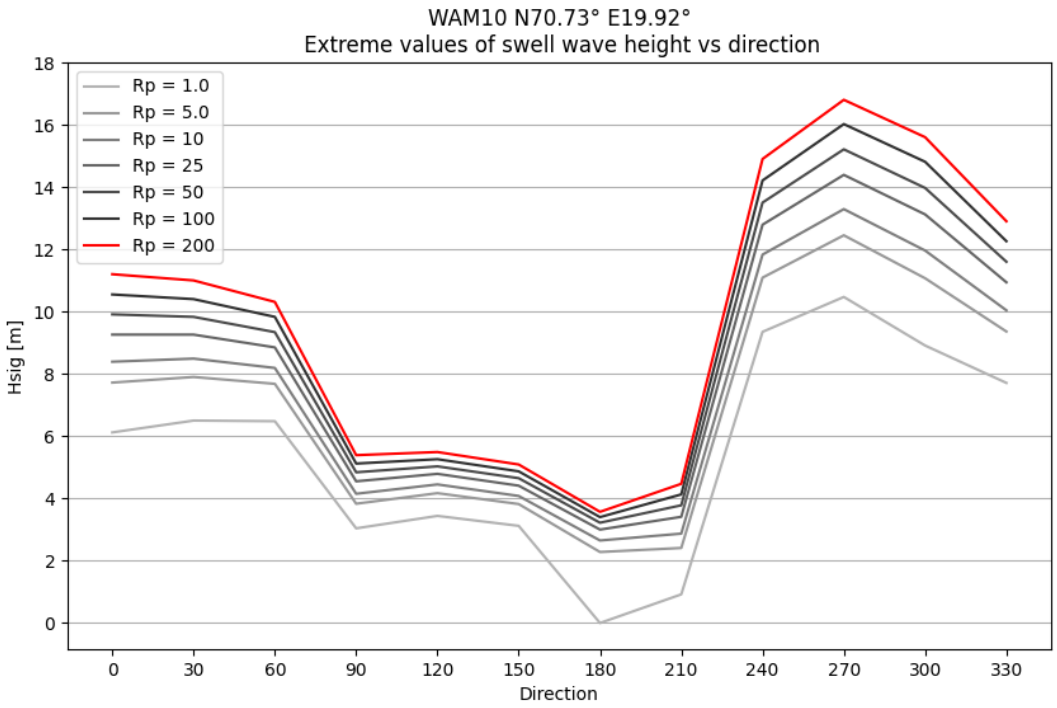

Figure 5.1: Overview of hindcast data from WAM10. Rp = return period

Direction	Significant wave height, Hsig [m]	Peak period, Tp [s]
240	14.9	16
270	16.8	18
300	15.6	17
330	12.9	15
0	11.2	14
30	11.0	14
60	10.3	14
90	5.39	12

Table 5.1: Wave parameters for a 200 year return period

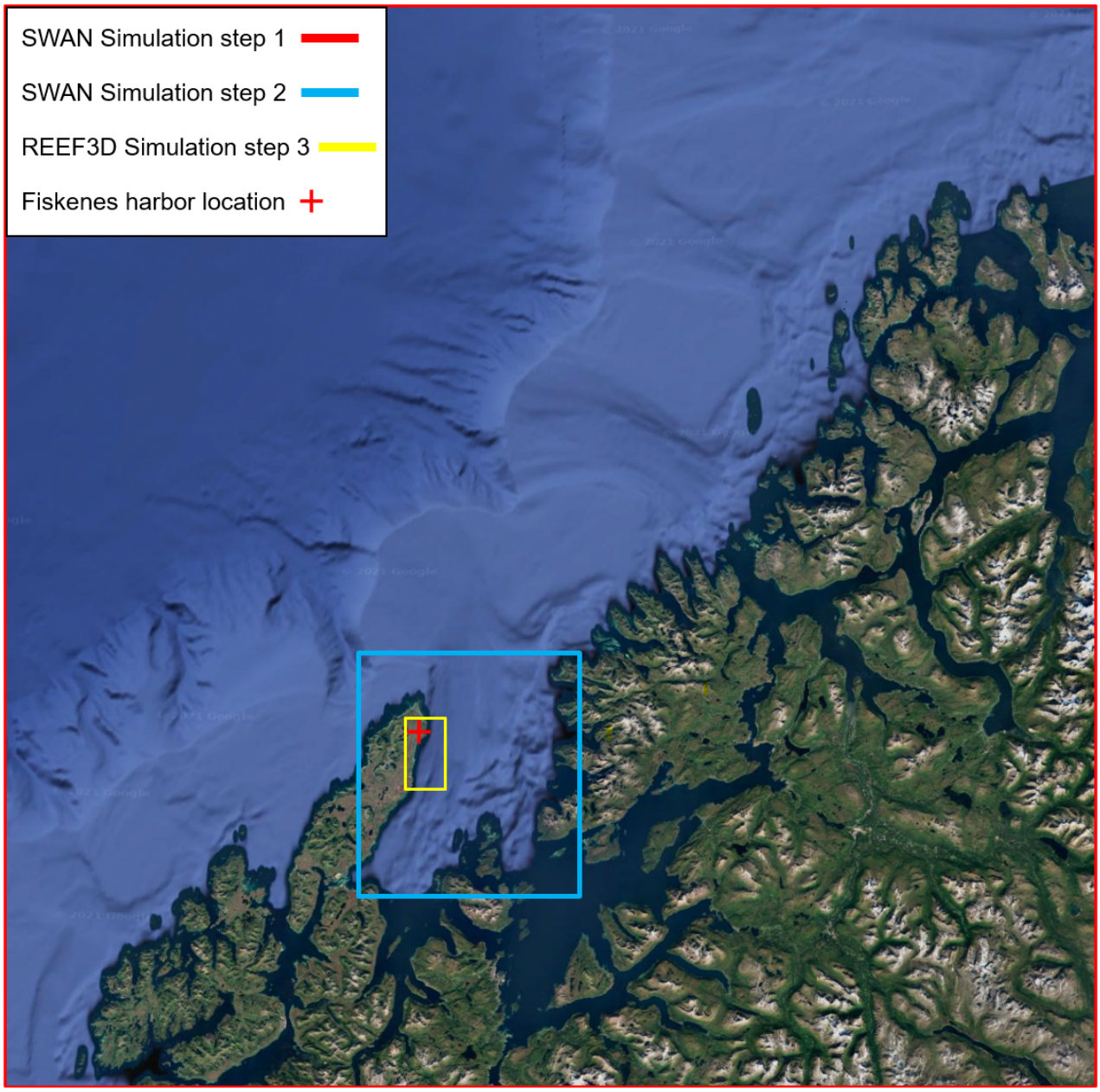

Figure 5.2: Simulation domain 1-2-3

SWAN Parameter	ON/OFF
Whitecapping (deep water wave breaking)	ON
Depth induces wave breaking	ON
Diffraction	ON
Refraction	ON
Triad wave-wave interaction	ON
Quadruplet wave-wave interaction	OFF

Table 5.2: SWAN simulation parameters

5.2.1 Simulation parameters in SWAN

SWAN does not simulate the free surface, but since the first iteration of the model was developed in 1994 (SWAN [2020]), many empirically calculated parameters have made the model able to better estimate different wave transformations. Some of the SWAN non-linear wave-wave interaction estimations are not accurate for some wave-states however. Notably, the quadruplet wave-wave interaction (four-wave interaction) was not used for the SWAN simulations in this thesis. The quadruplet wave-wave interaction are what generally dominate the evolution of the spectrum in deep water conditions, moving the energy from the low frequency components to the high frequency components of the spectrum SWAN [2020]. The reasoning for not including the effect for the SWAN simulations in this particular case is due to the long crested waves of the simulation, i.e. narrow directional distribution, where SWAN states that their approximation method gives poor results SWAN [2020]. Triad wave-wave interaction (three-wave interaction) however, where energy is transferred from higher frequencies to lower frequencies, have shown to have accurate approximations with long-crested waves (SWAN [2020]). An overview of what parameters were used in the SWAN simulations can be seen in Table 5.2.

5.2.2 Bathymetry

The consulting company obtained bathymetry data from the Norwegian public source Kartverket Kartverket [2021b] as well as from the EU initiative EMODnet EMODnet [2021] in areas bathymetry data was not available from Kartverket. The bathymetry data from Kartverket and EMODnet were used for Simulation steps 1 and 2 as seen in Fig. 5.3a and Fig. 5.3b. The bathymetry data for all the simulation steps are in reference to the Universal Transverse Mercator coordinate system (UTM), zone 33N.

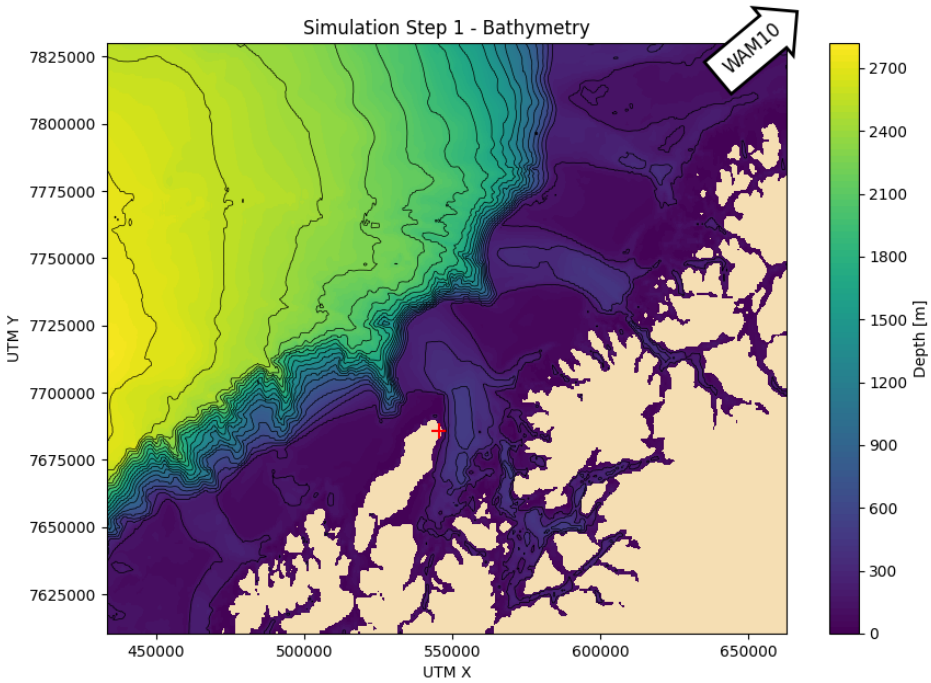

(a) Simulation domain 1

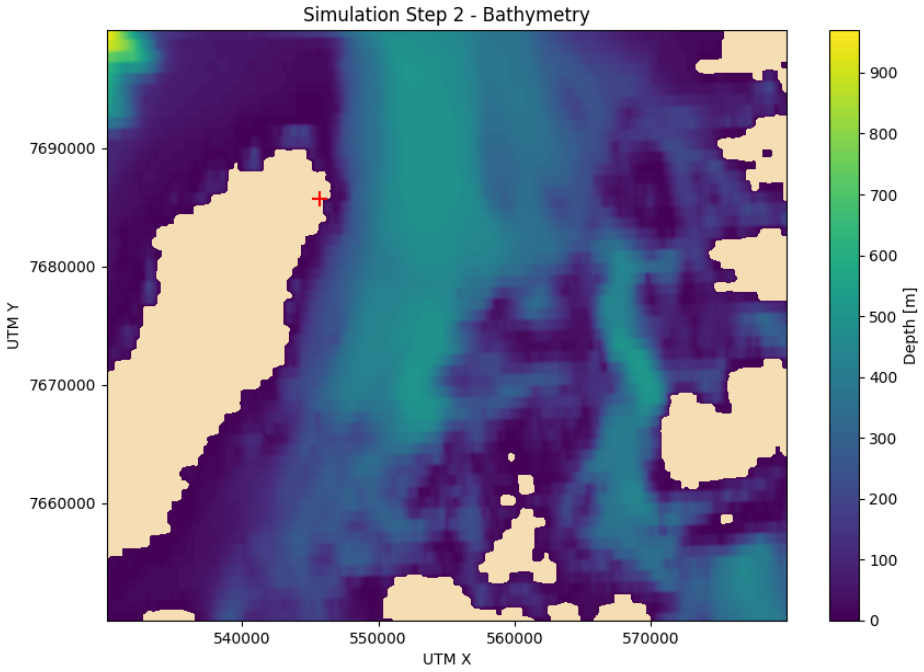

(b) Simulation domain 2

Figure 5.3: Bathymetry of the SWAN simulation domain

SWAN Simulation	X-extent [m]	Y-extent [m]	cell dx [m]	cell dy [m]
Step 1	229450	219700	458.9	439.4
Step 2	49875	49875	99.8	99.8

Table 5.3: SWAN simulation cell sizes

5.2.3 Simulation step 1

The first and largest, in terms of domain size, simulation was simulation step 1. The simulation domain was divided into a 500x500 grid, which gives cell sizes of approximately 450x450m^2, see Table 5.3. Initially, a total of seven simulations were run, one for each of the hindcast directions Table. 5.1. The input spectrum used for the SWAN simulations was a JONSWAP spectrum with a peak enhancement factor of 3.3.

5.2.4 Simulation step 2

In simulation step 2, the domain is divided into a 500x500 grid, resulting in cell sizes of approximately 100x100m^2, see Table 5.3. The resulting wave-state from simulation step 1 is used as an input into step 2 by using a nested approach.

Because the domain of simulation step 2 is encapsulated by the domain of simulation step 1, as shown in Fig. 5.2, one is able to extract wave spectrums along the whole boundary of simulation step 2 from the results of simulation step 1. 2000 unique directional spectrums along the boundary of simulation step 2, i.e. one unique directional spectrum/cell along the boundary, were extracted and serves as the input for the simulation. The effect of the nested approach can be seen in Fig. 5.4, where the significant wave height at the boundary of simulation step 2 is clearly non-homogeneous.

The same procedure that was conducted to extract the wave state around simulation step 2, was performed around the boundary of simulation step 3 for evaluation and further simulations in REEF3D::FNPF.

5.2.5 Interpolation of the simulation domain

It is very inefficient to run multiple simulations for all possible offshore wave directions. Therefore, in this study, it was conducted one SWAN simulation every thirtieth offshore wave direction between 240 and 90 degrees, as shown in Table 5.1. It is likely

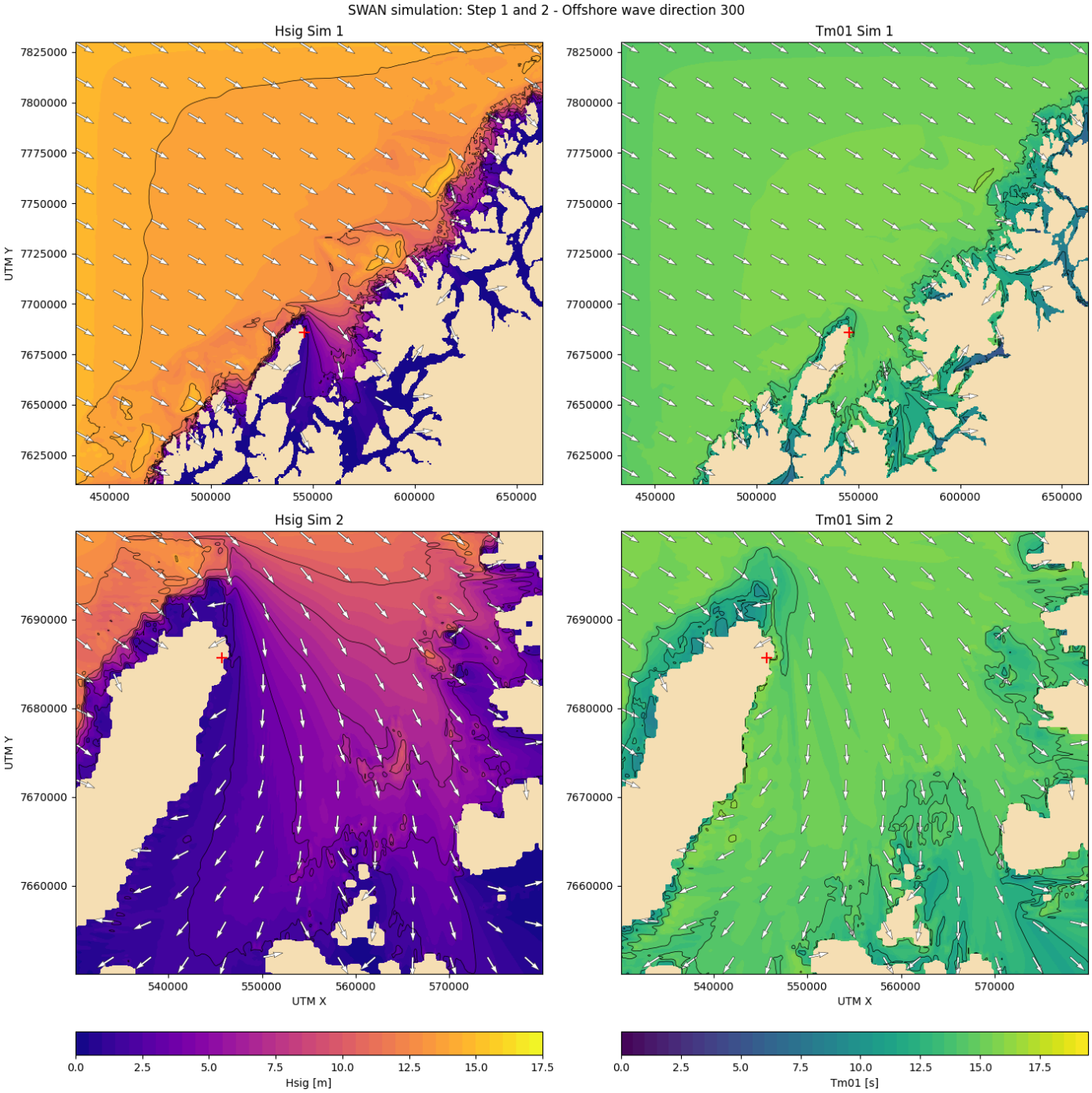

Figure 5.4: Significant wave height, peak period and mean direction for SWAN simulation Step 1 and 2 for offshore wave direction 300°

that the most adverse wave state is for an offshore wave direction between the simulations run. To analyze this possibility further, without needing to simulate every offshore degree between 240 and 90 degrees in SWAN, it was decided to interpolate the whole domain using the the results from the hindcast directions.

In SWAN, one is able to wave parameters such as significant wave height (H_s), peak period (T_p), and mean direction (θ_{mean}), for each cell in the simulated domain. By extracting these wave parameters for every cell in every simulated offshore wave direction case, one may estimate these parameters for the missing offshore wave directions by interpolating between the simulations. The interpolation method chosen was the cubic spline method which ensures a stable solution suitable for interpolating wave states without the oscillations that commonly occur when interpolating with higher-order polynomials (Pollock [1999]). To interpolate the mean direction, the mean directions were first converted into their respective unit vectors in the x- and y-direction then back to degrees, since interpolation with mean directions above and below 0 degrees becomes complicated.

5.2.6 The schematics of the interpolation process in the SWAN simulations

The interpolation process was conducted by interpolating every unknown direction on a cell-by-cell basis for the significant wave height, peak period, and the unit vectors of the mean direction, as is outlined in Fig. 5.5 and shown in Fig. 5.6. This results in four interpolation functions that are used to estimate the missing directions:

$$x_{unit}(i,j,\theta) = f_1(i,j,\theta) \tag{5.1}$$

$$y_{unit}(i,j,\theta) = f_2(i,j,\theta) \tag{5.2}$$

$$H_s(i,j,\theta) = f_3(i,j,\theta) \tag{5.3}$$

$$T_p(i,j,\theta) = f_4(i,j,\theta) \tag{5.4}$$

where, i and j indicate the cell position and θ indicates the offshore wave direction.

5.2.7 Verification of the interpolated values in SWAN

To verify the interpolated results, three additional runs are computed in SWAN with arbitrary offshore wave directions. The verification wave parameters are estimated from the hindcast data, Table 5.1, and gives the input for the verification simulations, Table 5.4.

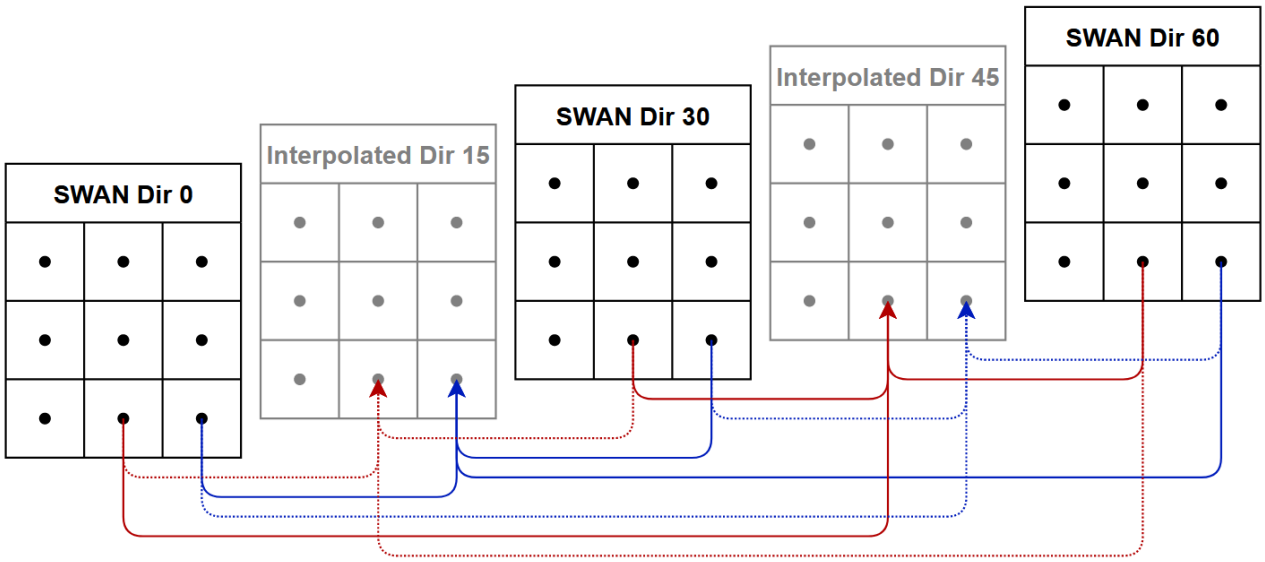

Figure 5.5: Simplified conceptual interpolation of 3x3 cell domain

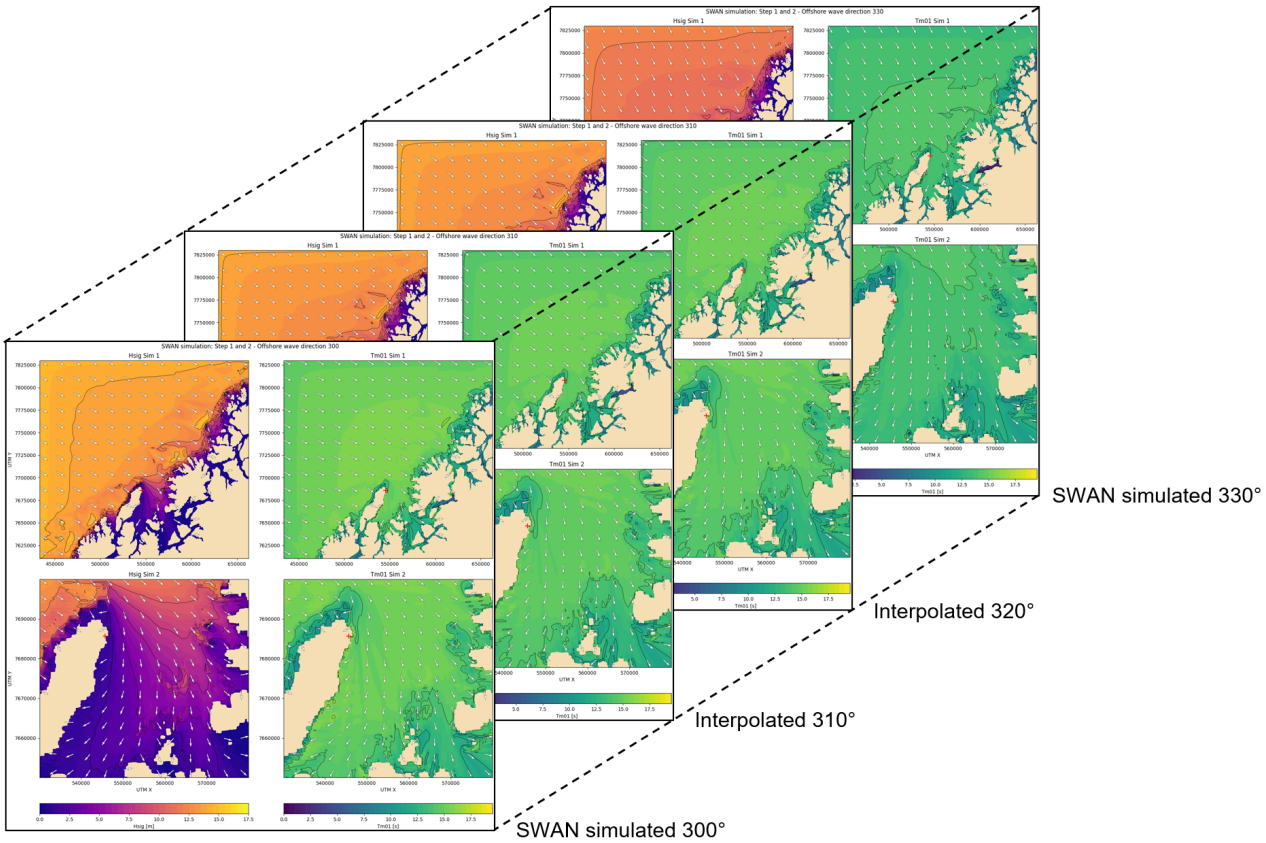

Figure 5.6: Interpolated sea-states in SWAN simulation

Direction	Significant wave height, Hsig	Peak period, Tp
281	16.36	17.63
18	11.08	14.0
36	10.86	14.0

Table 5.4: Wave parameters verification case in SWAN

To evaluate the accuracy of the cubic spline interpolation of the SWAN simulations, the mean absolute error, eq. 5.5, for three main parameters, significant wave height, peak period, and mean direction, was computed for every interpolated and simulated cell for each cell in the domain, see Table 5.5.

$$\text{MAE} = \frac{\sum_{i=1}^{n} |y_i - x_i|}{n} = \frac{\sum_{i=1}^{n} |e_i|}{n} \tag{5.5}$$

where MAE is the mean absolute error, x_i is the simulated value, y_i is the interpolated value, e_i is the error for cell i, and n is the number of cells in the domain.

The accuracy of the first two parameters, significant wave height and peak period, has an average error of below 1 percent. A difference of 1 percent is well within the expected accuracy of the SWAN model, meaning that for significant wave height and peak period, one may use the values for significant wave height and peak period from the interpolated wave state with sufficiently high confidence that the result from a SWAN simulation would be comparable.

The results for the mean direction of the interpolated cells are less accurate compared to the peak period and significant wave height, with an average mean error of 3.18 percent, see Table 5.5. The largest outlier is the interpolated offshore wave direction of 18°. It is expected that the lowest accuracy would occur for the offshore wave direction of 18° since, of the three verification cases run, it is the furthest from an actual simulated direction in SWAN. Due to the inaccuracy of the mean direction in some of the interpolated cases, the interpolated wave states for different offshore wave directions may not be used as inputs for the final REEF3D::FNPF simulation.

Although one may not use the results from the interpolated wave-states directly, it is a very efficient approach to access likely offshore wave directions that will inflict the most adverse wave conditions in the location of interest. When the offshore directions that likely will cause the largest waves are selected, one may run additional SWAN simulations for those specific cases to verify. The reason for the approach being well suited for determining the main offshore wave direction of interest is due to the computational efficiency. As seen in Table 5.6, efficient code in Python is able

SWAN Simulation domain	Domain 1			Domain 2			Average
Offshore wave direction	281	18	36	281	18	36	
Significant wave height - MAE [%]	0.41	2.54	0.67	1.08	0.82	0.29	0.97
Peak period - MAE [%]	0.71	0.58	0.51	0.53	0.31	0.41	0.51
Mean direction - MAE [%]	0.07	11.34	1.39	0.64	4.00	1.64	3.18

Table 5.5: Mean error difference between SWAN simulated and interpolated

	SWAN Simulation (1 Offshore wave direction)	Python Interpolation (210 Offshore wave directions)
Real time	291.3 sec	30.9 sec
CPU seconds	1149.9 sec	20.9 sec

Table 5.6: Comparison simulation time for one SWAN simulation and 210 interpolated offshore wave directions

to interpolate 210 offshore wave directions with 1.82 percent of the processor time required for just one SWAN simulation. Computing all offshore wave directions in SWAN, with one degree of accuracy, would take 11 554 times more CPU time than cubic spline interpolation of all the cells in Python.

5.3 REEF3D::FNPF Phase-resolved modeling

5.3.1 Bathymetry

For the final model step, near Fiskenes, additional measurements conducted by Secora AS (dated 12.07.19) were used in conjunction with the aforementioned bathymetry data obtained from public sources, see section 5.2.2, to increase the resolution of the bathymetry, see Fig. 5.7. The bathymetry data is in the coordinate system UTM 33N. The bathymetry of the simulation domain can be seen in 5.7. Note the drastic change in bathymetry east of Fiskenes and Breivik.

5.3.2 Topography

The topography data was obtained from the public Norwegian source Kartverket Kartverket [2021a] in the UTM33 N format with a 10-meter resolution in the x-y plane to match the UTM zone of the aforementioned bathymetry data. The open-source GDAL package GDAL [2021] is used to convert the original .tiff file from Kartverket to xyz format that only contains the coordinates of the data points. The vertical

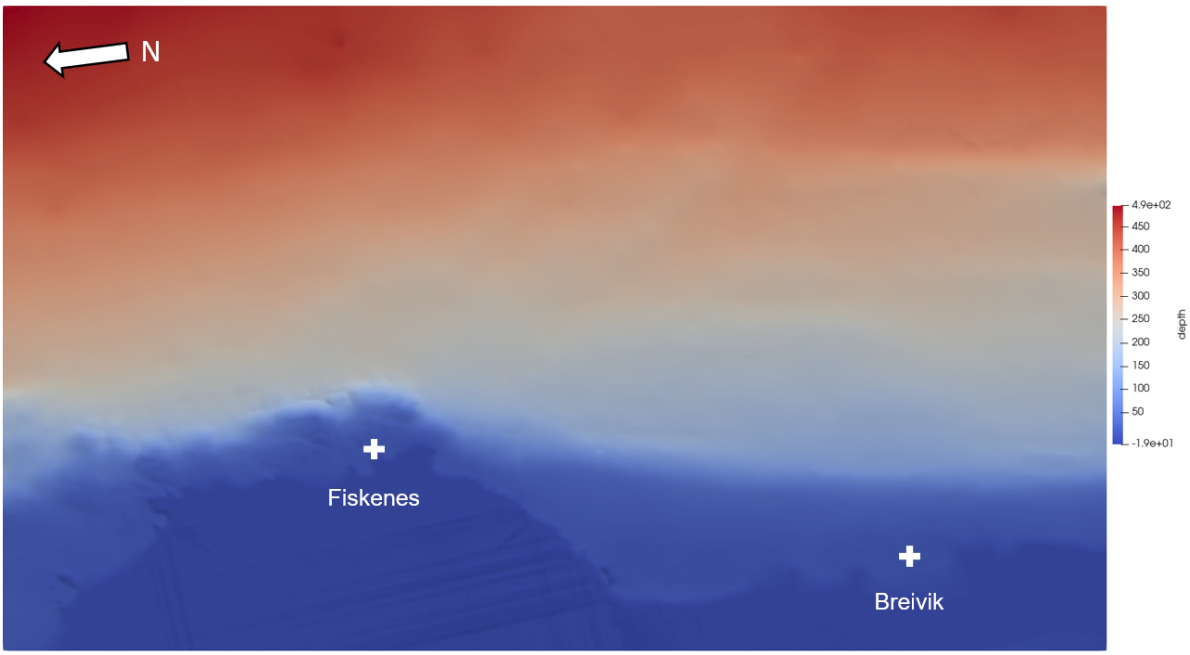

Figure 5.7: Bathymetry of REEF3D simulation. + marks the position of the original wave gauges

reference frame for topography data obtained from Kartverket is NN2000. The difference between the vertical reference frame in the bathymetry data and NN2000 is 1.46m at the nearby location of Andenes airport. Before the topography data could be merged with the bathymetry data it had to be adjusted to match the vertical reference frame of the bathymetry data.

5.3.3 Rotating the domain

The bathymetry data is rotated in the REEF3D numerical wave tank so that the positive x-direction aligns with the incoming wave direction. There are two main advantages to rotating the domain to align with the mean wave direction. Firstly, it ensures that there is the whole of the domain will be "filled" with waves. Secondly, it enables the domain to be smaller and still encapsulate the areas of interest with wave generation in the whole domain. Reducing the size of the domain, in turn, reduces the required number of cells for a set cell size dx = dy. The number of cells in a simulated domain is discovered to be nearly linearly proportional to the computational resources required for simulation, so the motivation is large to reduce the size of the domain where possible. It was therefore decided to rotate the grid around the z-axis such that it aligned with the mean wave direction of the given simulation.

To rotate the domain the bathymetry data was shifted to be centered around (0,0), then rotated such that the x-axis was aligned with the mean wave direction. After the rotation matrix was applied to the bathymetry data, the domain was again shifted such that the lower left corner was set to (0,0). The rotation of the bathymetry were conducted with the following rotational matrix:

$$[x_\theta \; y_\theta \; z_\theta] = [x \; y \; z] \begin{bmatrix} \cos\theta & -\sin\theta & 0 \\ \sin\theta & \cos\theta & 0 \\ 0 & 0 & 1 \end{bmatrix} \tag{5.6}$$

where θ is the counterclockwise rotation angle around the z-axis.

The procedure of rotating the bathymetry also had to be conducted on all the wave gauges to ensure that their location relative to the bathymetry remains constant regardless of the rotation of the domain. As three different mean wave directions would be used in the wave generation, a total of three bathymetry data-sets were generated, one for each direction.

5.3.4 Grid refinement and vertical grid

The bathymetry near the chosen sites is very complicated including several reefs close to the surface and a complex shoreline. An aerial photo reveals this clearly, as shown in Fig. 5.8. The domain in model step four is approximately 7000 by 12 000 m^2, which is large, yet demands a dense enough mesh to ensure sufficient capture of reflection, refraction, and diffraction in the domain. A horizontal grid of $\delta x = \delta y = 8m$ is selected. This gives the total domain approximately 1.3 million cells in the horizontal plane.

A total of ten cells in the vertical plane is selected. In order to achieve a better solution for the free surface without needing to add more vertical grids, which would increase the demand for computational resources, a stretching function is applied. To ensure a denser vertical mesh near the free surface, as shown in 2.1, a stretching factor of 2.5 is selected with the following function:

$$\sigma_i = \frac{\sinh(-\alpha) - \sinh\left(\alpha\left(\frac{i}{N_z} - 1\right)\right)}{\sinh(-\alpha)} \tag{5.7}$$

where,
α = stretching factor
i = index for the grid point
N_z = total number of cells in the vertical direction

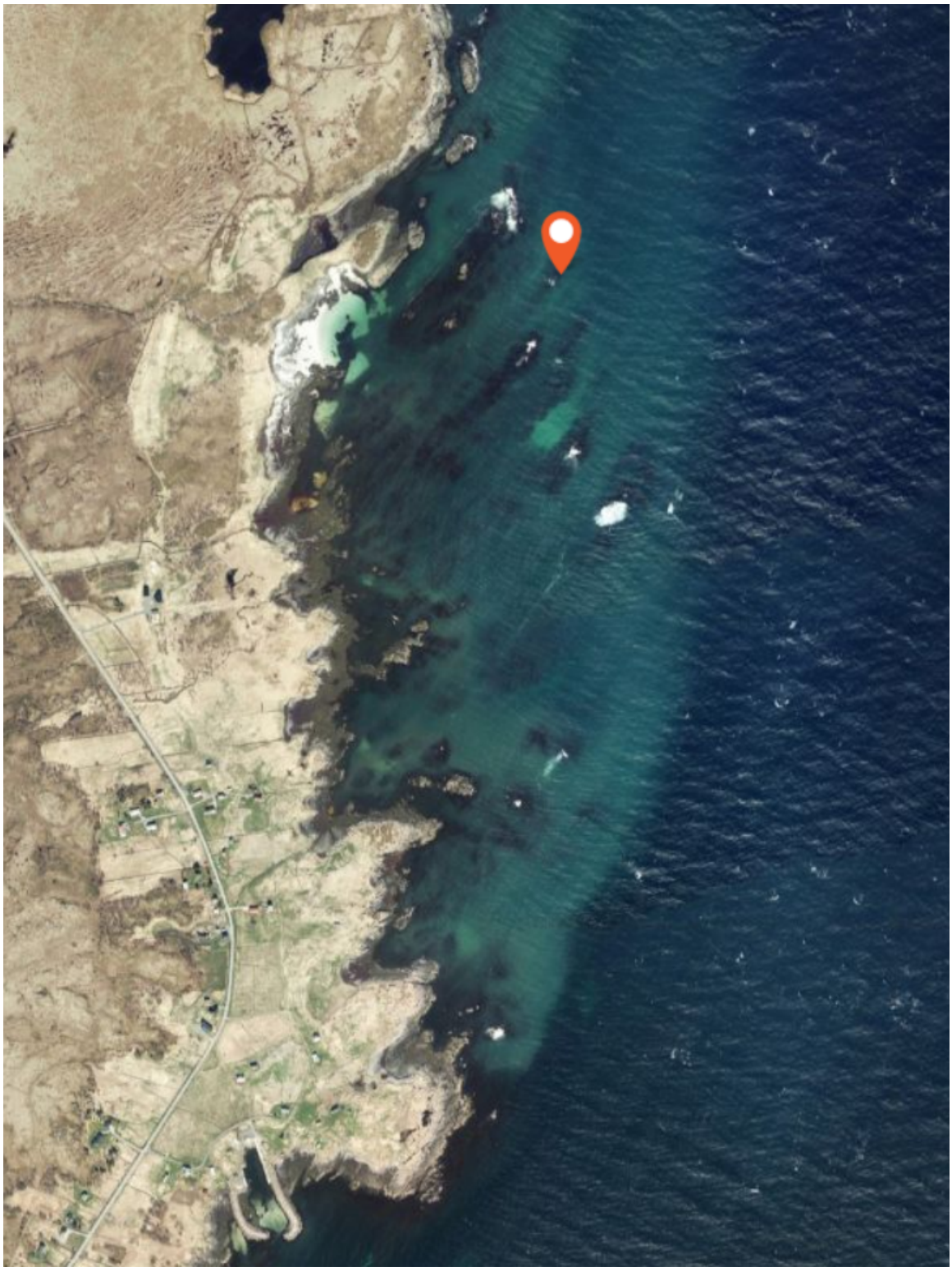

Figure 5.8: Fiskenes aerial photo, marker shows the proposed location of Fiskenes Harbour. source: Kartverket [2021a]

With ten cells in the vertical direction, the simulation is run with a total of 13.1 million cells.

5.3.5 Simulation duration

Because the study is considering irregular waves, a minimum simulation time of three hours is recommended. This is to ensure that there is sufficient time for the sea-state to develop as well as a reasonable estimate for the wave spectrum and the wave gauges to be calculated. When calculating the wave spectrum, the wave gauge data from the first twenty minutes will be ignored to ensure the initial development of the sea-state in the domain does not influence results. The REEF3D simulation will run on the supercomputer Fram using 256 cores.

5.3.6 Wave inputs

To decide what wave inputs to use in the REEF3D simulations, the output from the SWAN simulations was plotted along with the rand of the domain of the REEF3D simulation, as show for offshore 18 degrees in Fig. 5.9.

An overview of relevant wave parameters can be seen in Fig. 5.10 for the northeast corner of the SWAN simulation corresponding to the offshore wave direction used in the SWAN. It is observed, that for the SWAN simulations that produce the largest waves at the border of the REEF3D simulation, i.e. offshore wave directions between 330 and 40 degrees, see Fig. 5.10, the mean wave direction is within a very small directional band. Indeed, even for waves generated from 240 degrees, the wave direction at the northeast corner of the REEF3D simulation is 340 degrees, indicating severe wave transformation in the shallow waters north of Andøya. From Fig. 5.10, and an evaluation of the different border plots of the simulated offshore wave directions in SWAN, conclude that the SWAN offshore direction of 30 degrees is likely to cause the largest waves in Fiskenes and Breivik respectively. In addition, the interpolated values suggest that an offshore wave direction of 18 degrees may result in even larger waves at the location of Fiskenes harbor. Therefore, an additional simulation is run in SWAN to verify the interpolated result for an offshore wave direction of 18 degrees.

REEF3D is able to use user-defined uni-directional wave spectrum as inputs. A simple solution to generate a uni-directional spectrum from a multi-direction spectrum is by summing the wave action density and applying it for a single direction, then later apply directional spreading directly in the REEF3D simulation. This is not a good solution if there are swell waves and wind-generated waves from different

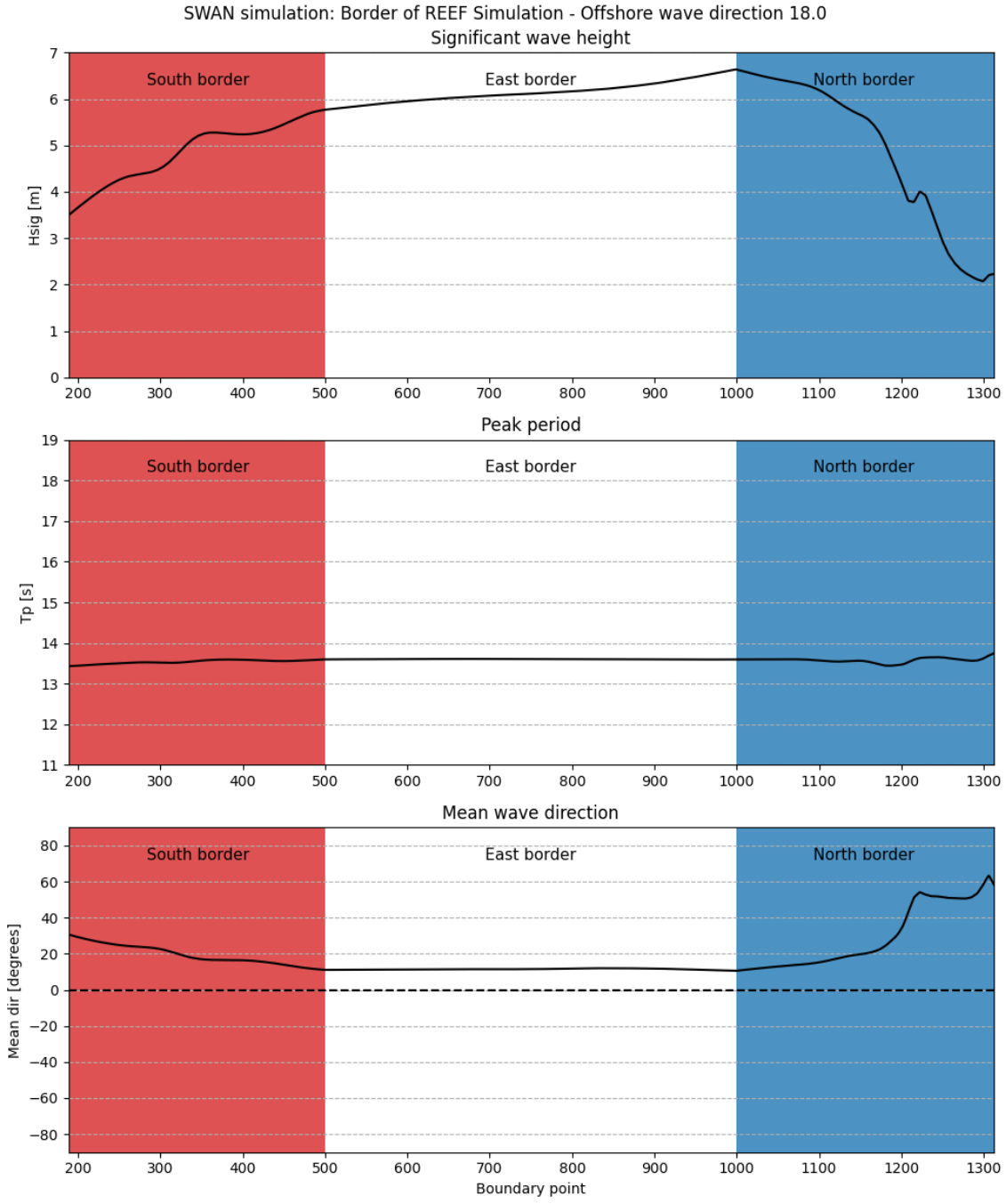

Figure 5.9: SWAN wave parameters along the boundary of the REEF3D simulation

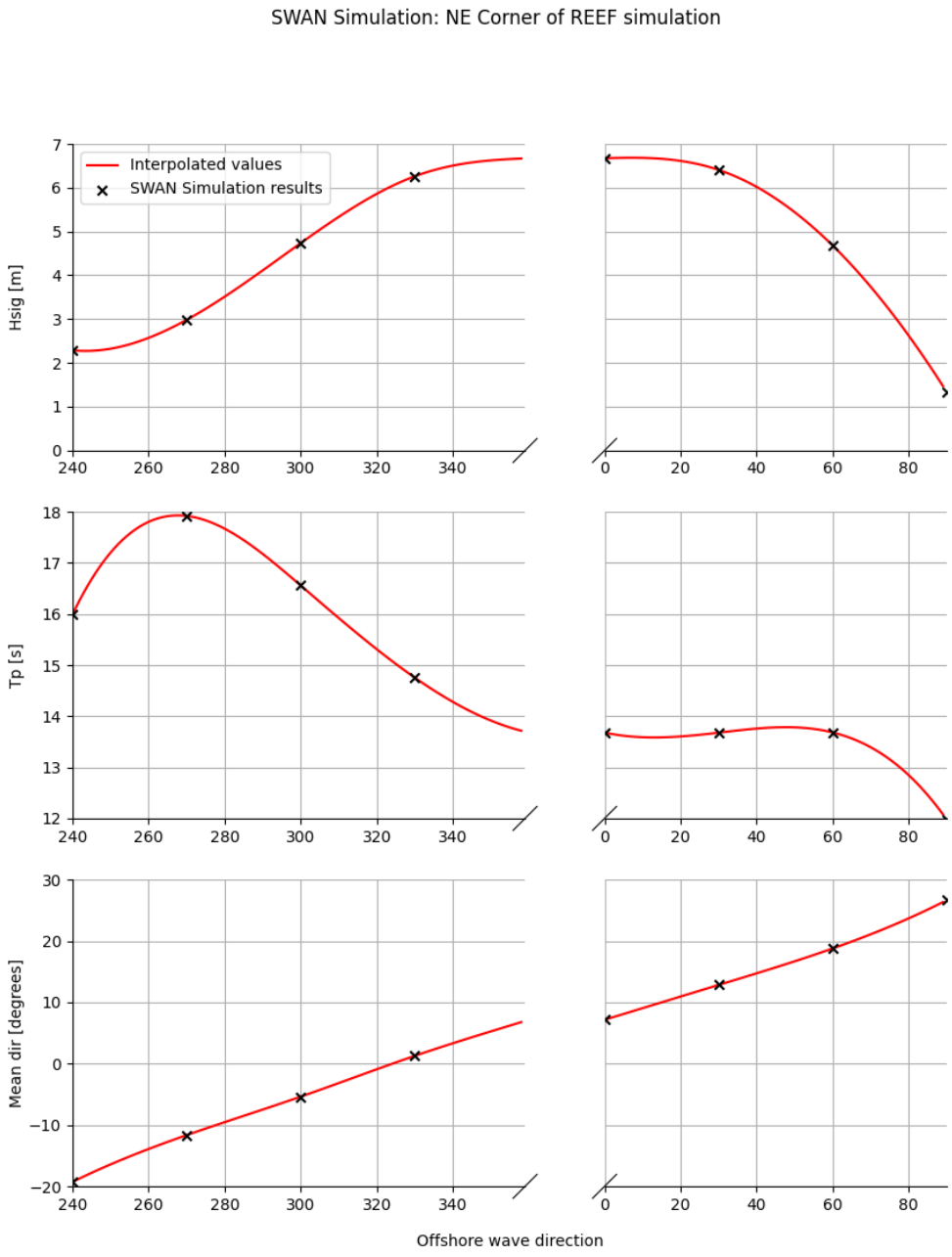

Figure 5.10: Significant wave height, peak period and mean direction values from SWAN simulation from the northeast corner of REEF3D simulation

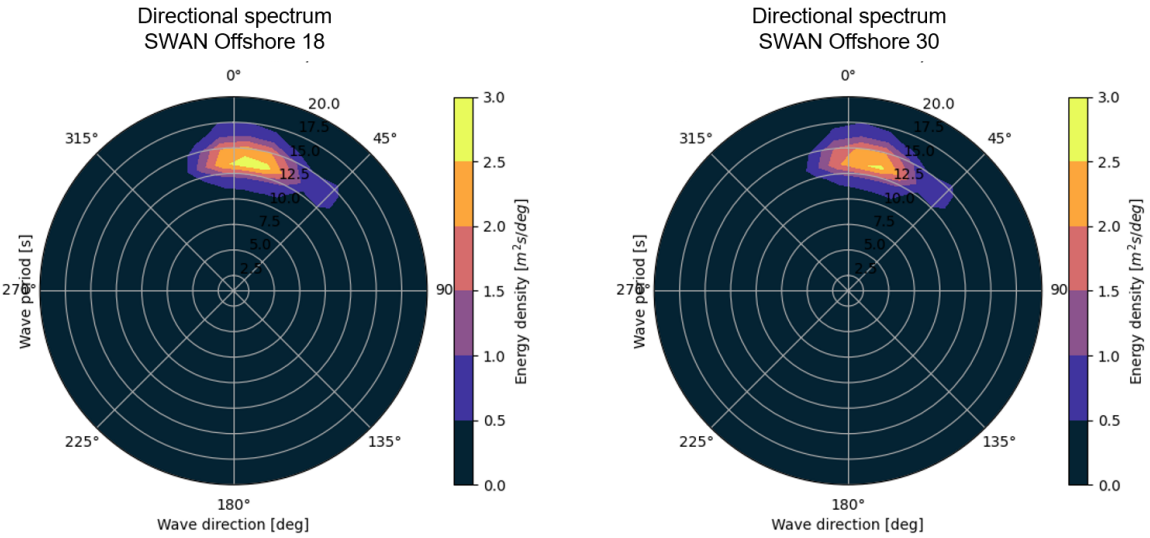

Figure 5.11: SWAN directional spectrum at the NE corner of the REEF3D simulation domain

SWAN Simulation Offshore direction	REEF3D Simulation	Significant wave height	Peak period	Mean direction	Directional spreading
0	Sim 1	6.67 m	13.7 s	7.1°	ON
18	Sim 2	6.67 m	13.7 s	10.7°	ON
30	Sim 3	6.41 m	13.7 s	12.8°	ON
30	Sim 4	6.41 m	13.7 s	12.8°	OFF
30	Sim 5*	6.41 m*	13.7 s	12.8°	OFF
*Sim 5 uses regular wave with H of 6.41 m					

Table 5.7: Wave parameters for input uni-directional input spectrums in REEF3D

directions, but as seen in Fig. 5.11 this is an acceptable solution for this specific modeling case. The wave energy is concentrated within a narrow directional band and there are no wind-generated waves.

The input spectrum in REEF3D are shown in Fig. 5.13 and wave parameters corresponding to the input spectrums of the full-scale simulations in REEF3D are summarized in Table 5.7. To ensure the input spectrums are realistic, the corresponding JONSWAP spectrum is plotted with the equivalent values for significant wave height and peak period, with a peak enhancement factor of 3.3, see Fig. 5.13.

Recall from section 5.2.4, that simulation step 2 of the SWAN simulation gives an output of 2000 directional wave action spectrums along the boundary of the REEF3D simulation domain. From the multi-directional wave spectrum, one is able to extract

the significant wave height, peak period, and mean wave direction.

5.3.7 Wave generation and numerical beach

In order for REEF3D to accurately generate and dissipate waves, it is known that the wave generation zone and numerical beach must be approximately one wavelength. For the REEF3D simulations, the peak period is approximately 14 seconds, see Table 5.7. Using the intermediate formula for wave-length, wave-period relation from linear wave theory, eq. 5.8, at the deepest point in the domain, 505 meters, a wavelength of 306 meters is estimated. In this study, a wave generation zone length of 400 meters is used to cover one wavelength corresponding to the peak period and take into consideration the lower frequency long wave components.

$$\lambda = \frac{g}{2\pi} T^2 \tanh \frac{2\pi h}{\lambda} \tag{5.8}$$

where g is the gravitational acceleration, T is the wave period, h is the water depth, and λ is the wavelength.

5.3.8 Spectrum from REEF3D wave gauges

REEF3D is a phase-resolved model, which means that it's not as simple as extracting the directional spectrum from a cell that can be done in spectral wave models such as SWAN. REEF3D::FNPF generates a free surface in the simulated domain, and as such, it is able to provide free surface elevation in time domain for wave gauges. In order to generate a uni-directional spectrum from a time series of a free surface elevation wave gauge, a Fast Fourier Transform (FFT) analysis may be used. There are several packages that will compute this quite efficiently, the common scipy package **fft** was used for the analysis in this thesis. FFT analysis requires a set sampling frequency, and since the sampling frequency of the REEF3D wave gauges are tied to the time step in the REEF3D simulation, it is not necessarily a fixed value. To satisfy the condition of a constant sampling frequency, the time series of the free surface was interpolated using a simple one-dimensional interpolation scheme and an interpolated time series with a sampling frequency of 25Hz generated.

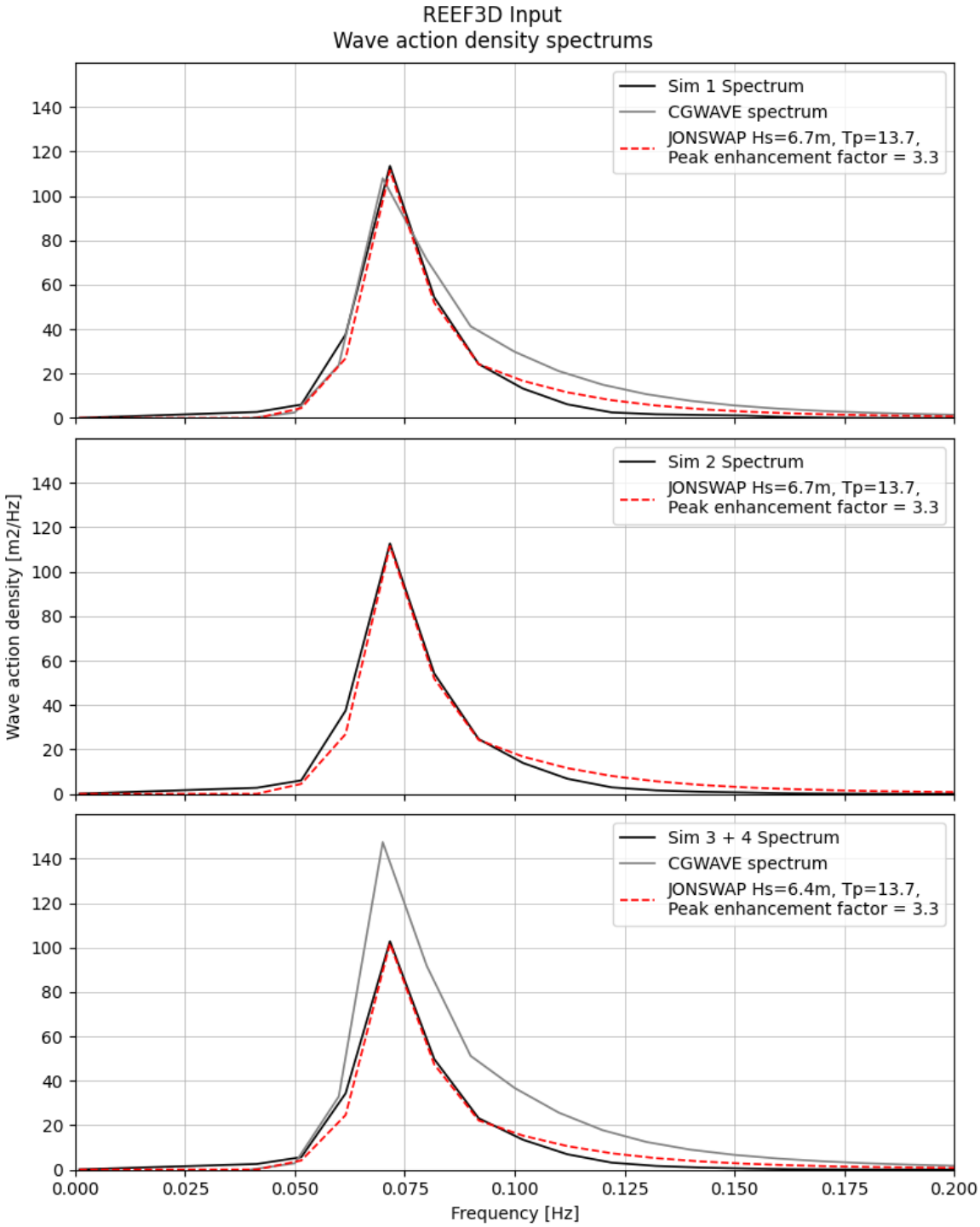

Figure 5.12: Input wave action density spectrums in REEF3D Simulation

The significant wave height, H_s, and the mean wave height, H_{mean}, needed for simulation 5 due to the regular waves, was calculated using the following formulas:

$$m_0 = \int_0^{f_c} S(f)\, df \tag{5.9}$$

$$H_s \approx H_{m_0} = 4\sqrt{m_0} \tag{5.10}$$

$$H_{mean} \approx \frac{1}{\sqrt{2}} H_s \tag{5.11}$$

where m_0 is the 0th order moment of the wave action energy spectrum, and f_c is the cutoff frequency, set at 5 Hz.

5.3.9 Wave gauges

In order to generate a map of the significant wave height and the peak period wave gauges were set in a 70x70 grid in the simulation domain for a total of 4900 wave gauges (the upper limit of the number of lines in control files is 5000), and are shown in Fig. 5.13. After the REEF3D simulation was completed, the analysis in outlined in section 5.3.8 was conducted on all the wave gauges. The first 2000 seconds of the analysis were removed to let the sea-state fully develop before the FFT analysis was run.

In addition to the numerical wave gauges needed to generate the significant wave height map, additional wave gauges were set up to match those of the consulting firm for comparison. The consulting firm had one wave gauge at the proposed location of each harbor, in addition to these, five more gauges were added upstream of the wave propagation direction meaning North and North-East of the original wave gauge. The UTM location of each wave gauge in addition to their relative location to the two original wave gauge locations in Fiskenes and Breivik can be seen in Table 5.8.

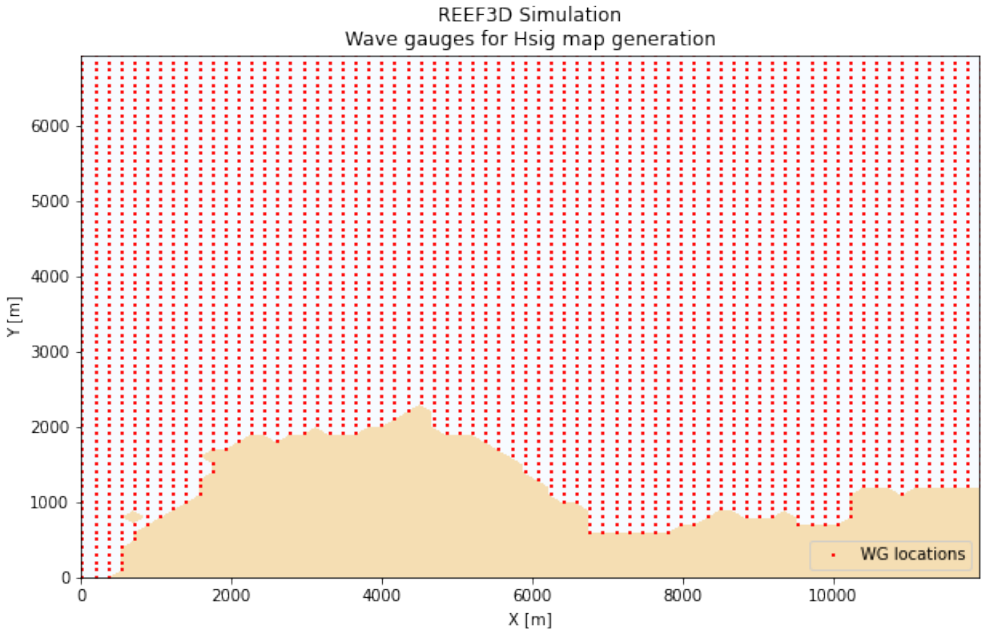

Figure 5.13: Wave gauge grid for generation of significant wave height map

REEF3D Wave gauge	UTM 33N X [m]	UTM 33N Y [m]	dx [m]	dy[m]
WG1 Fiskenes	546655	7685293	+0	+0
WG2 Fiskenes	546755	7685293	+100	+0
WG3 Fiskenes	546855	7685293	+200	+0
WG4 Fiskenes	546755	7685393	+100	+100
WG5 Fiskenes	546855	7685493	+200	+200
WG6 Fiskenes	547155	7685793	+500	+500
WG7 Breivik	544391	7678434	+0	+0
WG8 Breivik	544591	7678434	+200	+0
WG9 Breivik	544491	7678434	+100	+0
WG10 Breivik	544491	7678534	+100	+100
WG11 Breivik	544591	7678634	+200	+200
WG12 Breivik	544891	7678934	+500	+500

Table 5.8: Overview of the numerical wave gauges UTM location to access the wave conditions in Fiskenes and Breivik and their offset from the original wave gauges in the consulting firms analysis

Chapter 6

Study of wave properties in Fiskenes and Breivik

Simulation 1 is a test case with 0-degree northern waves. However, according to SWAN analysis from Fig. 5.11, most waves come from northeastern directions, thus simulations 2-5 are more representative cases and will be the focus of this thesis. Disregarding simulation 1, we have four wave simulations that are performed with four distinct wave input scenarios. In the REEF3D simulations, waves are generated from the left-hand side boundary and dissipated at the numerical beach to the right as seen in Fig. 6.1. In addition to the numerical beach, energy is also dissipated in the coastal relaxation zone of 16 meters to avoid wave run-up and give a more realistic reflection property of the coastline.

The REEF3D::FNPF simulations ran on the supercomputer Fram with 256 cores for approximately 15 hours, the CPU usage is outlined in Table 6.1.

6.1 REEF3D Simulations

Due to the phase-resolved approach of REEF3D::FNPF, one is able to visualize the free surface in the time-domain explicitly. The ability to reconstruct the free surface

REEF3D Simulation	CPU cores	Simulation time
Sim 2	256	14:57:14
Sim 3	256	15:38:23
Sim 4	256	16:38:35
Sim 5	256	14:09:32

Table 6.1: Overview of elapsed time for the REEF3D simulations

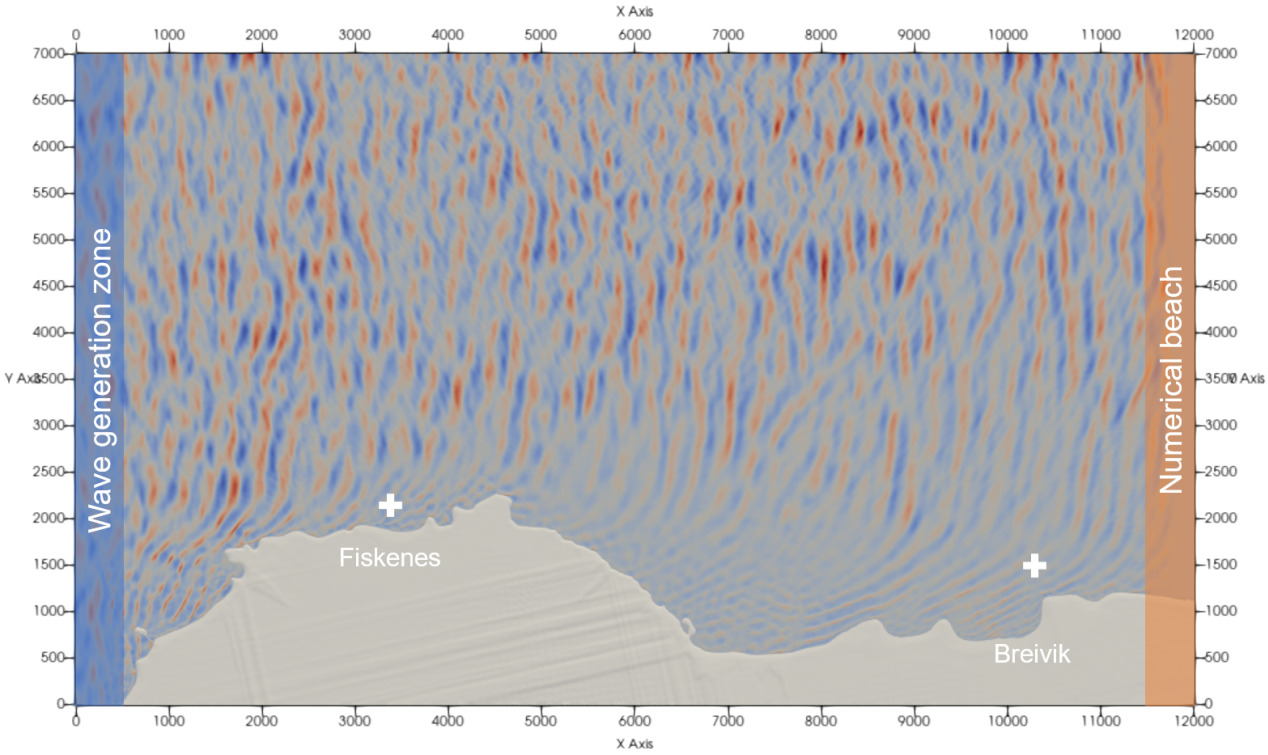

Figure 6.1: Numerical wave tank configuration in the REEF3D simulations. The wave generation zone is located at the left-hand side boundary and the numerical beach is at the right-hand outlet boundary. The wave gauges for the evaluation of the two sites are marked with white cross. The dimensions of the domain are in meters.

is advantageous as it gives information about wave physics not possible with phase-averaged models. The visualization software used for the analysis of the REEF3D simulations is the open-source software Paraview. The free surface at 10 000 seconds simulation time with different principal wave directions can be seen in Fig. 6.2 and Fig. 6.3.

For the REEF3D simulations with directional spreading, simulations 2 and 3, the domain is completely filled with waves, and the waves seem to be dissipated well at the numerical beach. Short-crested waves are seen in the offshore area in the upper half of the computational domain, where the wave propagation is less influenced by the bathymetry changes and coastlines. However, strong shoaling and diffraction take place near the coastline as water depth becomes smaller and waves propagate into the sheltered region. Longer waves have a stronger capability to bypass obstacles and show stronger diffraction patterns. As a result, long-period waves form a long-crested wave field in the diffraction zone, as seen between the two chosen sites.

Simulation 4 is performed with irregular wave field without directional spreading as shown in Fig. 6.3a. In this case, a long-crested wave field is observed in the entire numerical wave tank. Here, all waves of different frequencies travel in the same direction and experience strong diffraction. As a result, it seems to be smaller waves in the sheltered area to the short-crested wave case, where more waves are able to propagate into the area between the sites from different angles. In the top right corner of the simulation 4 Fig. 6.3a, there are indications of reflecting waves from the numerical beach. Following the practice of the industry partner, a regular wave scenario is also investigated, see Fig. 6.3b. Since the generated waves propagate with one frequency and direction, the effects of wave-boundary interaction and wave-wave interaction are more visible as shown in Fig. 6.3b. The diffracted wave and the incident wave interact and show alternating high energy field and low energy field as the waves propagate over the tip of the peninsula.

In the area between Fiskenes and Breivik significant diffraction is occurring and the waves are turning toward the shielded area behind Fiskenes, see Fig. 6.2 and Fig. 6.3. The effect of diffraction is also very clear from the significant wave height maps, as when diffraction occurs, the wave action density, m^2/Hz, is distributed over a larger area, as shown in Fig. 6.4. Shoaling near Fiskenes is very prevalent, and is most clearly seen in the simulation 5 with regular waves, see Fig. 6.3b. Shoaling also occurs in the steep bathymetry change, see Fig. 5.7, south of Fiskenes. Wave breaking near Fiskenes is also prevalent due to reefs and shallow water, which is clearly visible in Fig. 5.8.

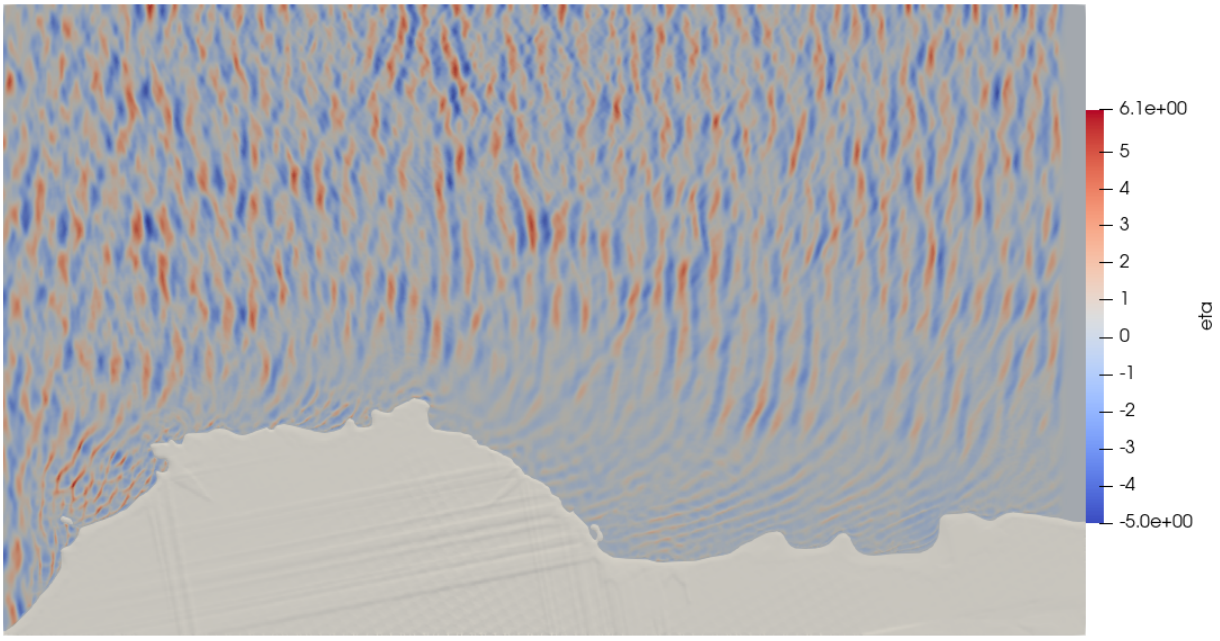

(a) REEF3D Simulation 2 - Free surface elevation (eta, in meters)
$\theta_{mean} = 10.7°$, $H_s = 6.67m$, $T_p = 13.7s$

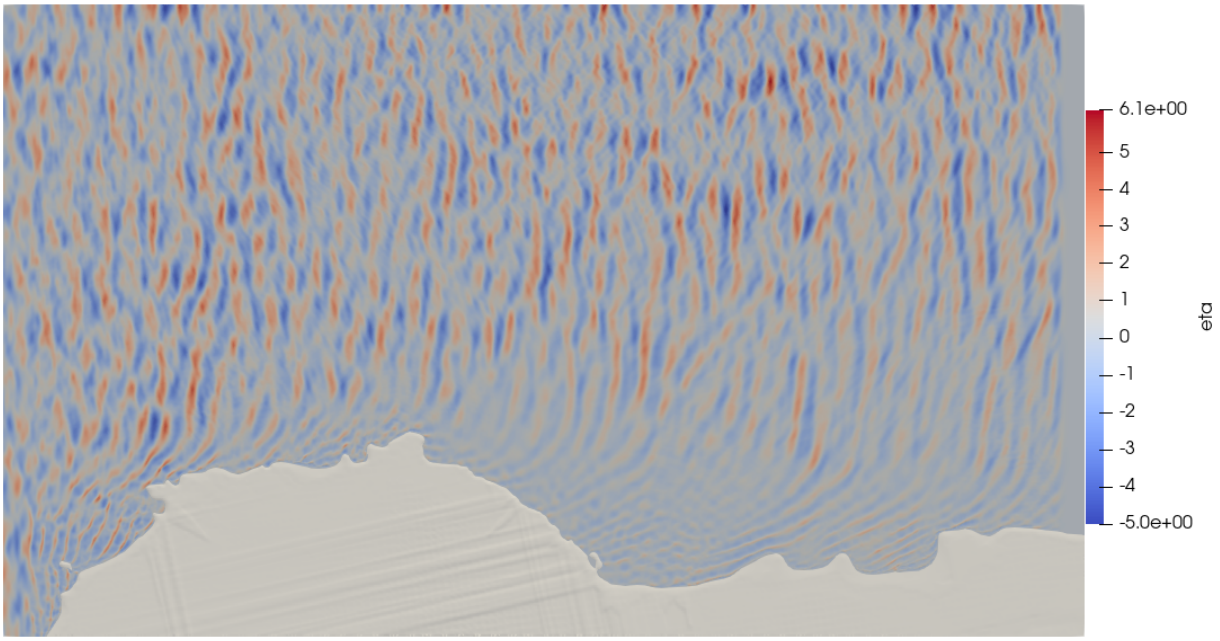

(b) REEF3D Simulation 3 - Free surface elevation (eta, in meters)
$\theta_{mean} = 12.8°$, $H_s = 6.41m$, $T_p = 13.7s$

Figure 6.2: REEF3D Simulations free surface elevation visualized in Paraview

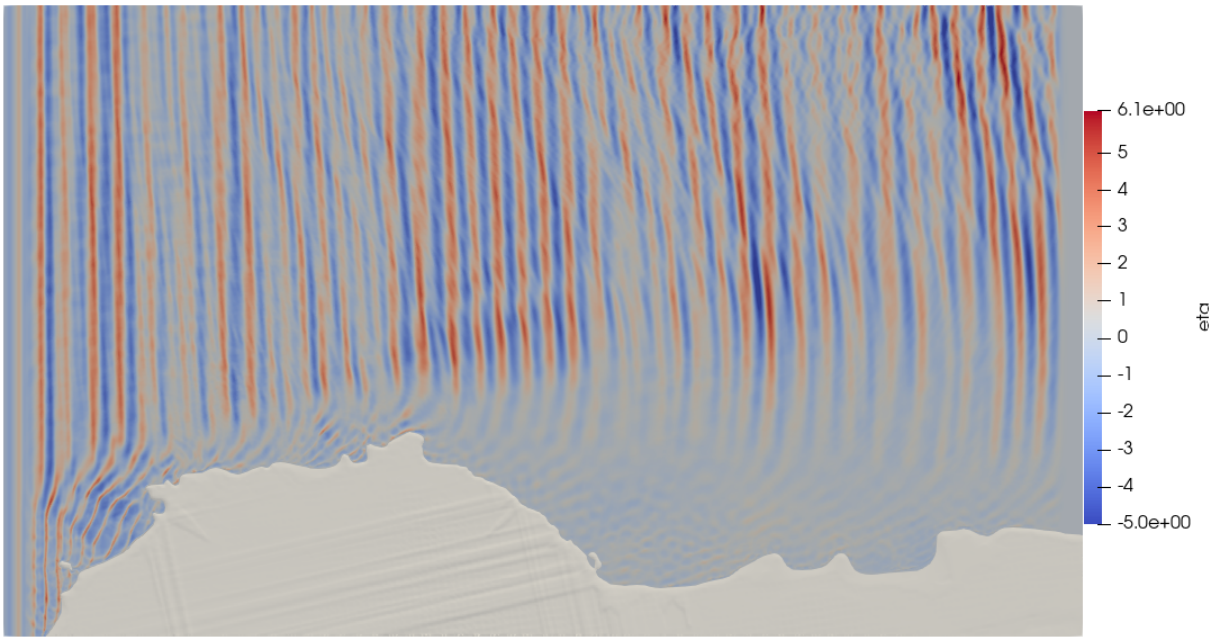

(a) REEF3D Simulation 4 - Free surface elevation (eta, in meters)
$\theta = 12.8°$, $H_s = 6.41m$, $T_p = 13.7s$

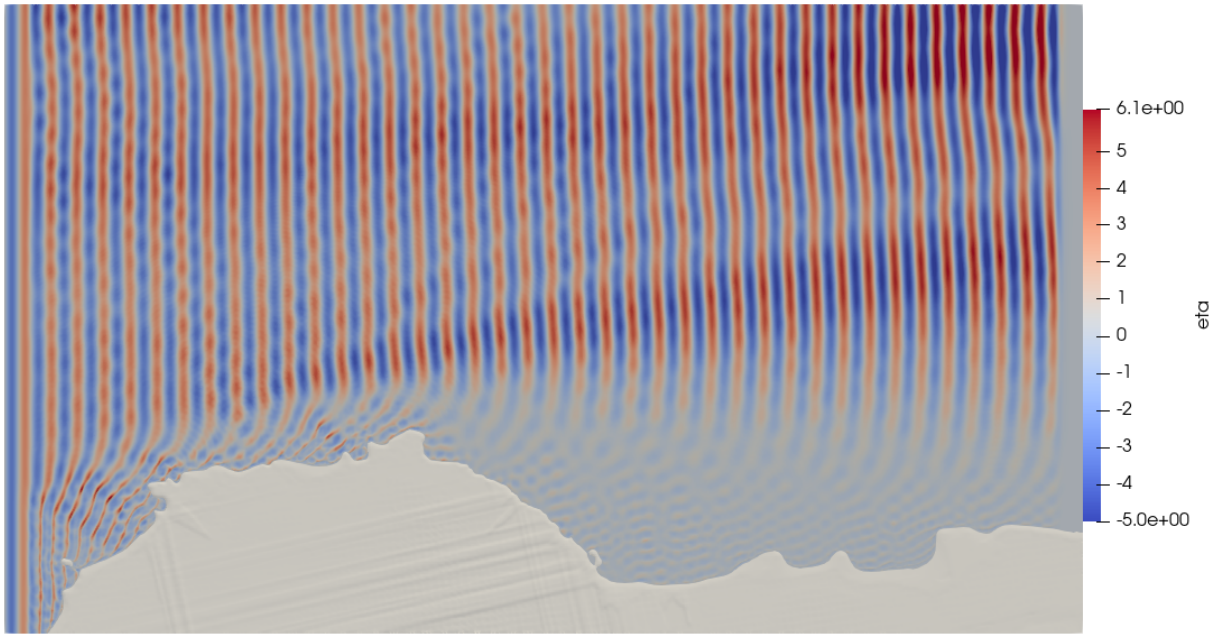

(b) REEF3D Simulation 5 - Free surface elevation (eta, in meters)
$\theta = 12.8°$, $H = 6.41m$, $T_p = 13.7s$

Figure 6.3: REEF3D Simulations free surface elevation visualized in Paraview

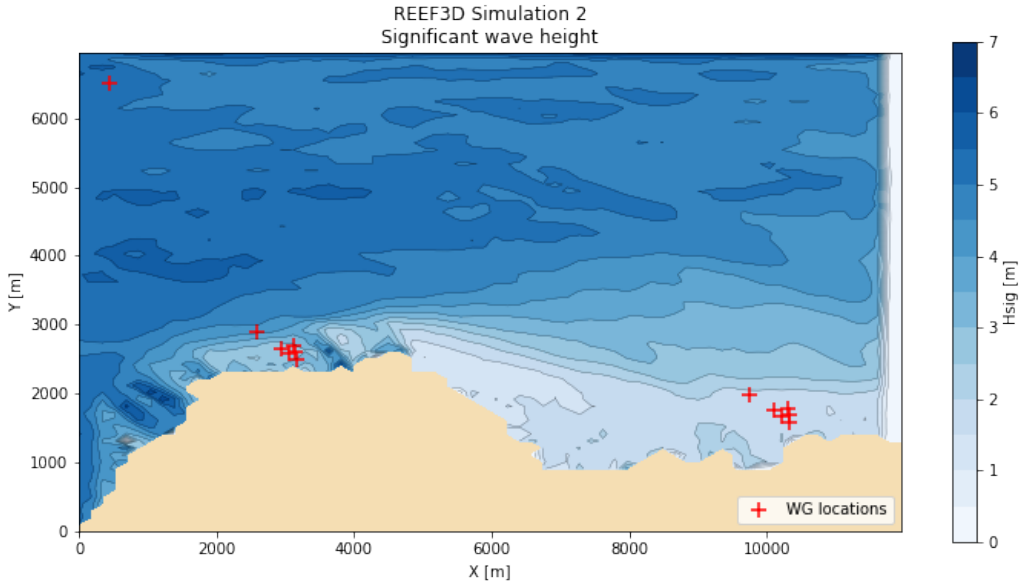

(a) REEF3D Simulation 2 - Significant wave height
$\theta_{mean} = 10.7°$, $H_s = 6.67m$, $T_p = 13.7s$

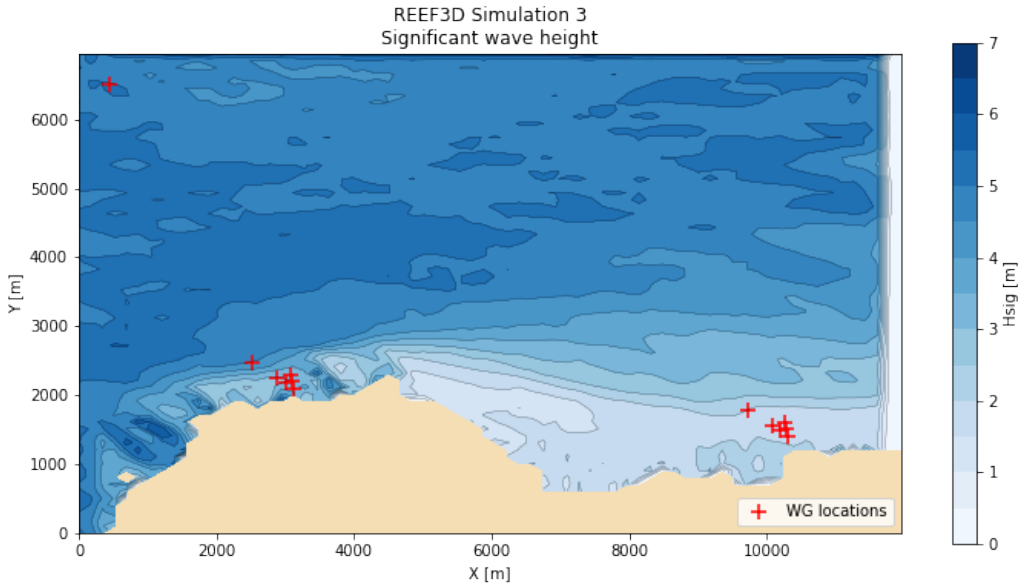

(b) REEF3D Simulation 3 - Significant wave height
$\theta_{mean} = 12.8°$, $H_s = 6.41m$, $T_p = 13.7s$

Figure 6.4: H_s map from REEF3D simulations

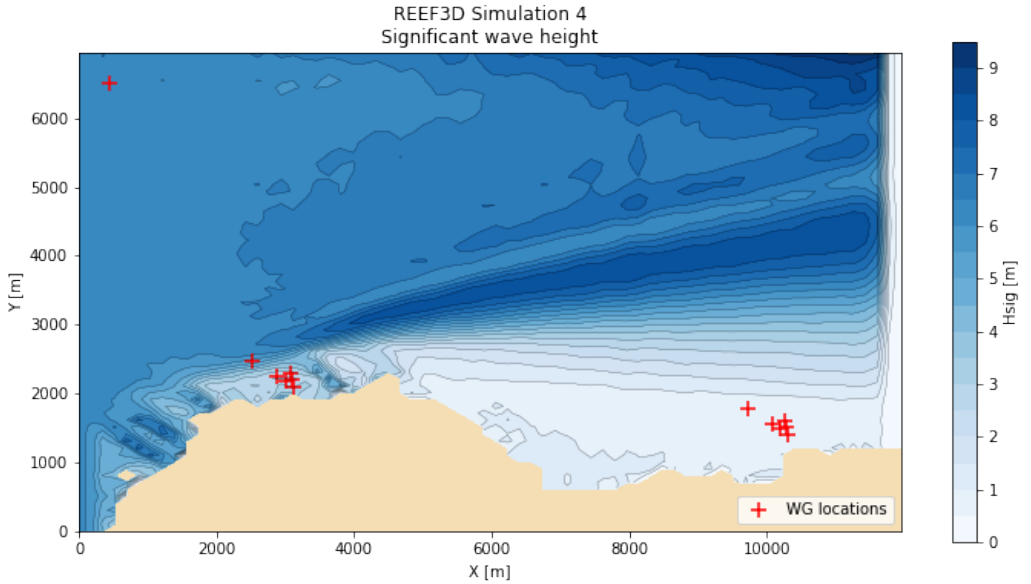

(a) REEF3D Simulation 4 - Significant wave height
$\theta = 12.8°$, $H_s = 6.41m$, $T_p = 13.7s$

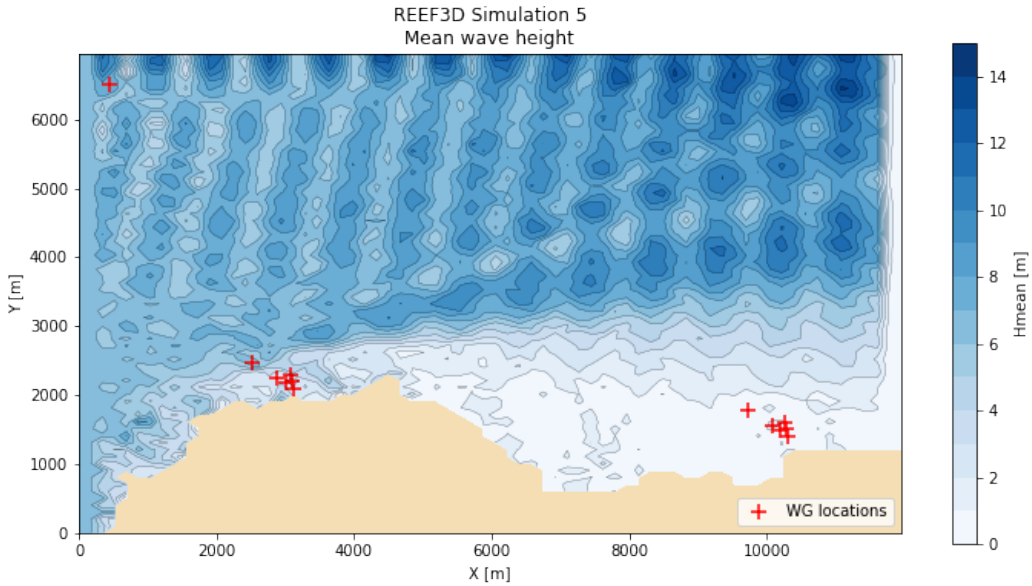

(b) REEF3D Simulation 5 - Mean wave height
$\theta = 12.8°$, $H = 6.41m$, $T_p = 13.7s$

Figure 6.5: H_s and H_{mean} map from REEF3D simulations

REEF3D Simulation		Sim 2	Sim 3	Sim 4	Sim 5
Wave gauge #	Depth [m]	H_s [m]	H_s [m]	H_s [m]	H_{mean} [m]
WG Wave generation	505.38	5.39	5.09	6.25	7.86
WG1 Fiskenes	12.4	2.62	2.90	2.41	0.95
WG2 Fiskenes	18.2	2.69	3.01	2.55	1.11
WG3 Fiskenes	30.9	2.99	3.23	2.88	3.31
WG4 Fiskenes	19.8	2.72	2.87	2.52	1.53
WG5 Fiskenes	35.6	2.63	2.89	2.46	1.79
WG6 Fiskenes	147.8	4.16	4.46	5.25	4.02
WG7 Breivik	15.4	1.60	1.74	0.70	0.76
WG8 Breivik	28.8	1.67	1.74	0.67	0.59
WG9 Breivik	21.2	1.61	1.73	0.68	0.85
WG10 Breivik	19.6	1.60	1.68	0.68	0.80
WG11 Breivik	25.5	1.64	1.76	0.65	1.10
WG12 Breivik	53.3	1.79	1.98	0.68	0.79

Table 6.2: Significant wave height at wave gauges from the REEF3D::FNPF simulation cases and the water depth at the wave gauges

In theory, the generated waves near the generation boundary should be spatially homogeneous at the deep water condition. However, variations of H_s are observed in the multi-directional irregular wave case, see Fig. 6.10, which causes the differences in H_s when compared to the uni-directional irregular wave shown in Fig. 6.8a. Due to the multi-directional nature, it is possible that some wave traveling in the eastern direction are partially reflected from upper boundary, which leads to in-homogeneity in the wave field. In the simulation with regular wave input, a periodic variation of H_s is observed along the x-direction. Here, since there is only one frequency in the wave field, possible reflected waves from the numerical beach at the right-hand outlet boundary may lead to a standing wave pattern. It is recommended to use a longer numerical beach in future studies. For the unidirectional irregular wave simulation, there is almost no reflection from the upper boundary, different frequency components have different reflection properties and do not have as strong an impact on the overall wave propagation as in the case of the regular waves.

6.2 Site-specific analysis

6.2.1 Fiskenes

Fiskenes is more exposed to swell waves from northerly directions than Breivik. The deep waters also continue quite close to the proposed location of Fiskenes harbor meaning that large wave transformations are occurring very close to the proposed harbor area. As can be seen from 6.2, and the bathymetry in 6.6, wave gauge 1 and wave gauge 6 are only about 700 meters apart, but the water depth at the wave gauges are 12.4m and 147.8m respectively. The steepness of the bathymetry between the wave gauges gives a sea-bed slope of approximately 1:5, sure to induce severe shoaling and possibly wave breaking that in turn dissipates wave energy. The dissipation of energy is clearly shown by the reduction of significant wave height in all simulation cases, see Fig. 6.7 and Fig. 6.8.

Simulation 2 and 3, corresponding to the met-ocean spectral analysis of offshore waves from 18 and 30 degrees respectively, gives an H_s of 2.62 m and 2.90 m. Wave gauge 6, which is only 700 m northeast, gives results for H_s of 4.16 m and 4.46 m for the two simulations. Interestingly, the cases with directional spreading, results in higher significant wave height for all wave gauges except wave gauge 6, see Table 6.2. Directional spreading allows more waves to propagate towards the site at different angles and leads to less diffraction. In contrast, strong diffraction takes place for waves of all frequencies in the unidirectional wave scenario, which possibly leads to the lower wave height at the more sheltered regions where wave gauges 1-5 are located.

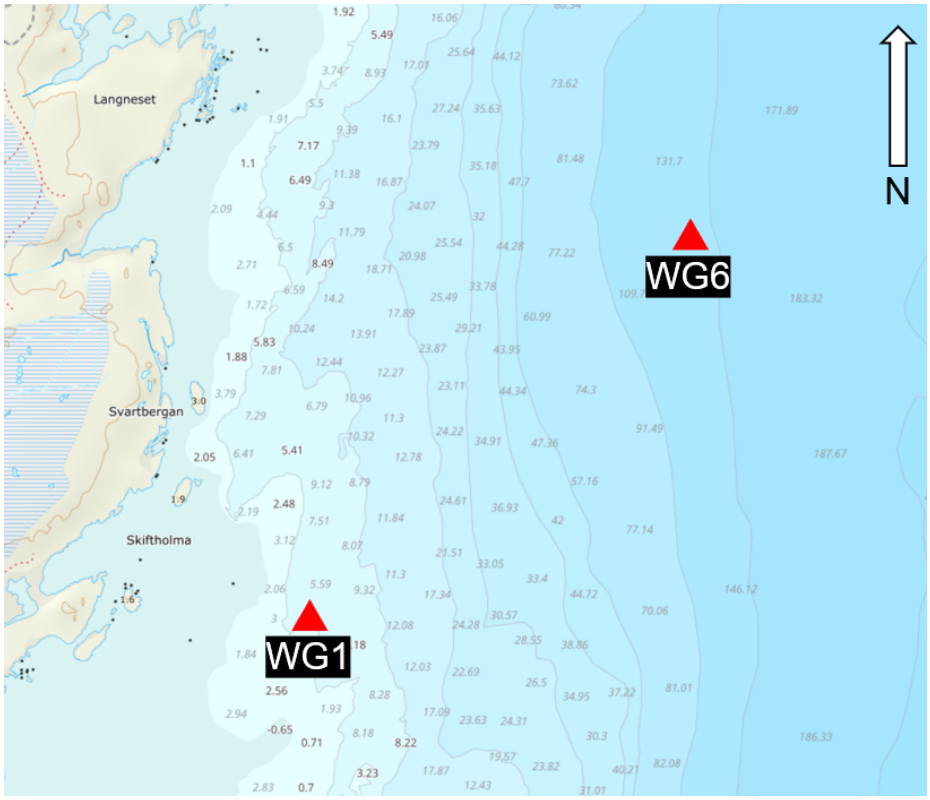

Figure 6.6: Bathymetry and location of WG1 and WG6 near Fiskenes

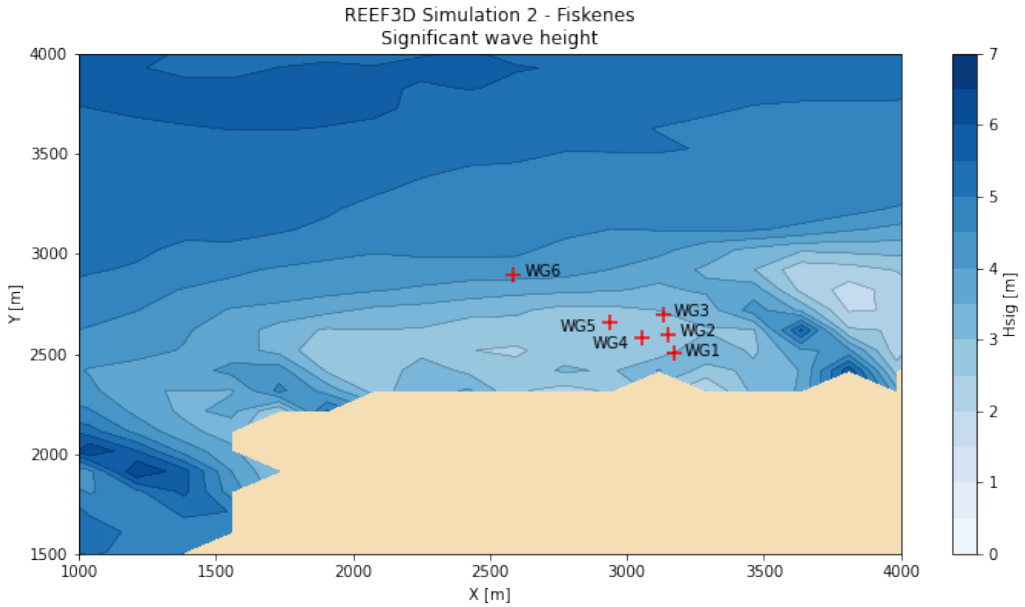

(a) REEF3D Simulation 2 - Significant wave height
$\theta_{mean} = 10.7°$, $H_s = 6.67m$, $T_p = 13.7s$

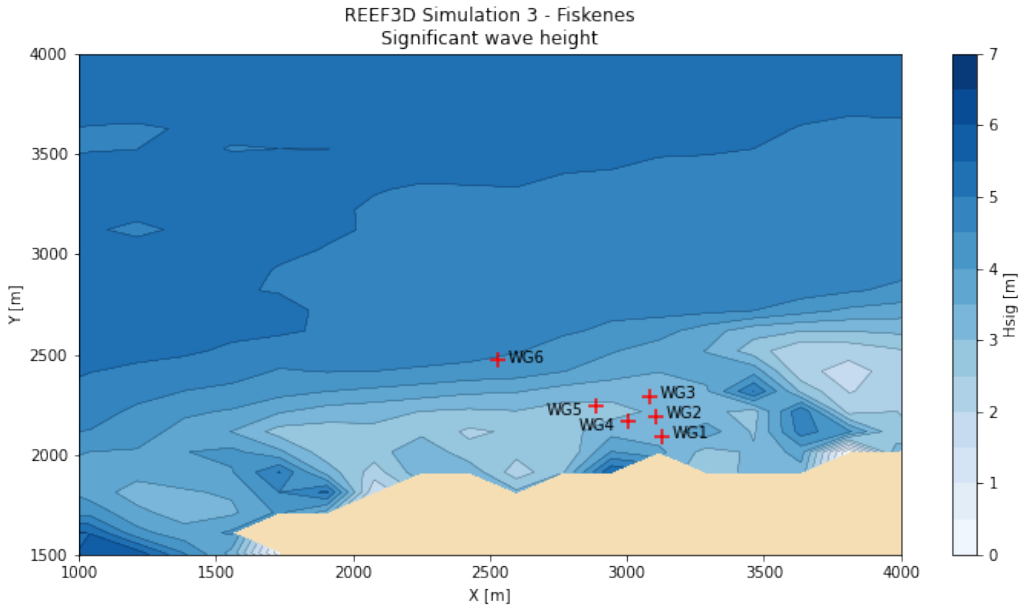

(b) REEF3D Simulation 3 - Significant wave height
$\theta_{mean} = 12.8°$, $H_s = 6.41m$, $T_p = 13.7s$

Figure 6.7: H_s map from REEF3D simulations

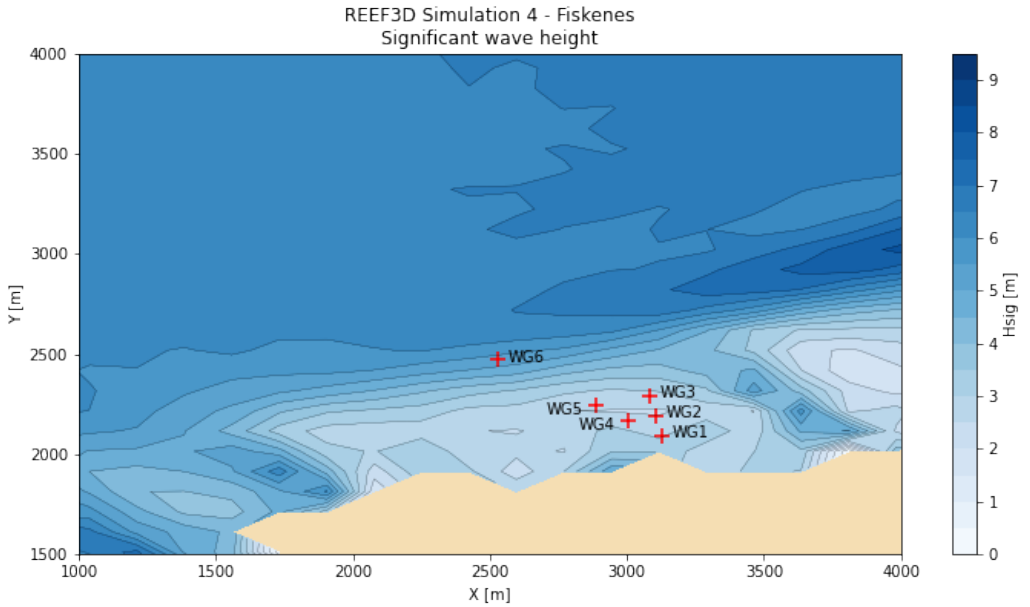

(a) H_s map Simulation 4
$\theta = 12.8°$, $H_s = 6.41m$, $T_p = 13.7s$

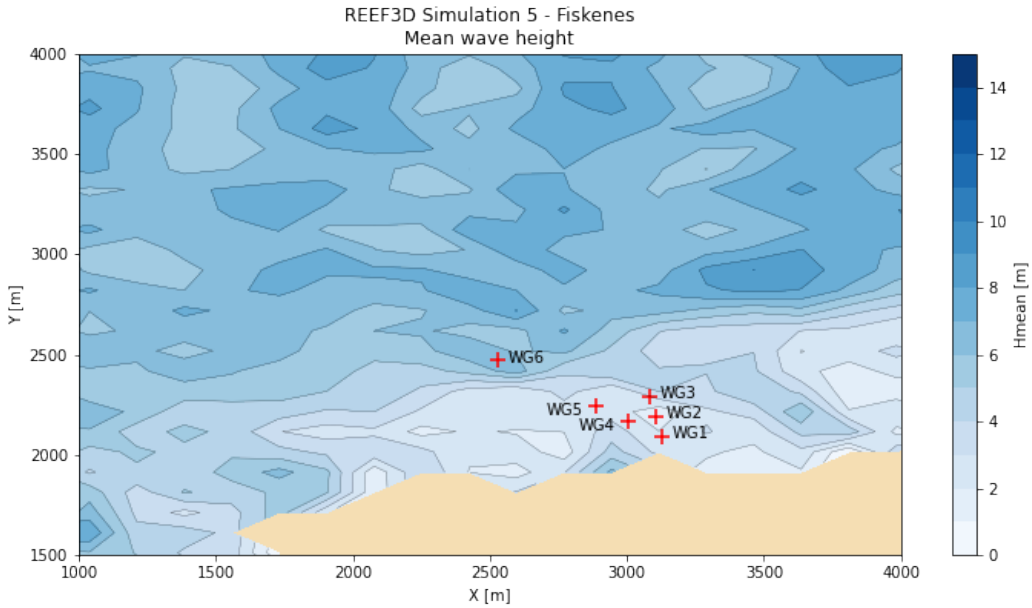

(b) H_s map Simulation 5
$\theta = 12.8°$, $H = 6.41m$, $T_p = 13.7s$

Figure 6.8: H_s and H_{mean} map from REEF3D simulations

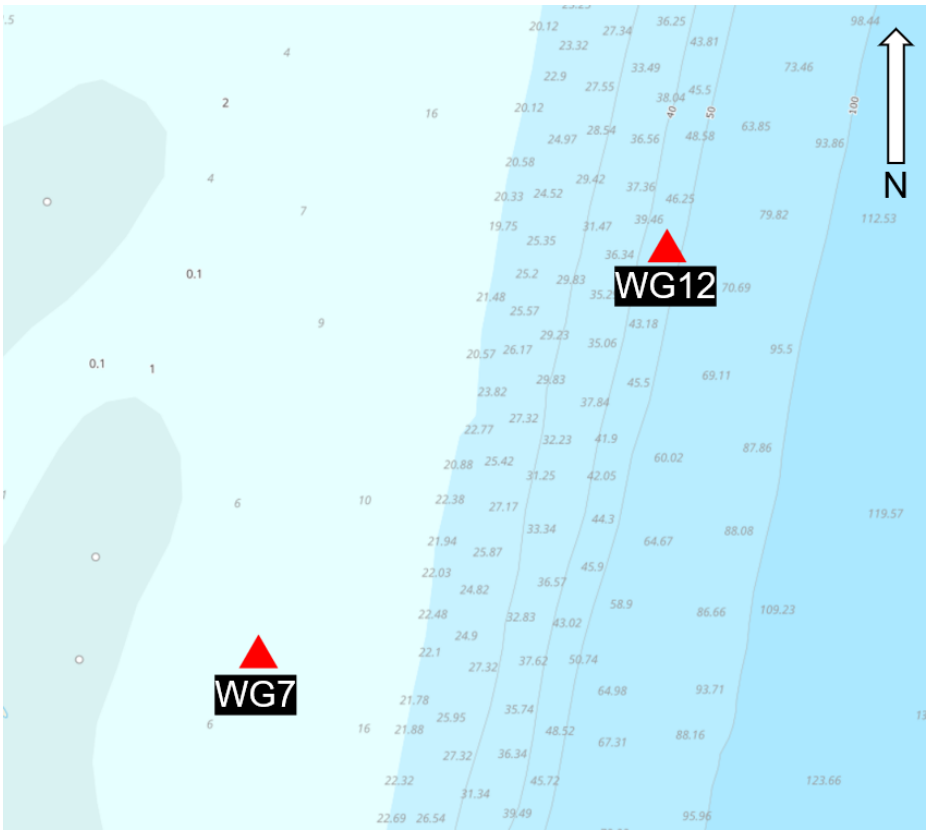

Figure 6.9: Bathymetry and location of WG7 and WG12 near Breivik

6.2.2 Breivik

Breivik is very sheltered from waves propagating from the north due to the coastline stretching eastward north of the area, see 5.7. There is a clear depth difference between the wave gauges, although the slope is significantly shallower than in Fiskenes. The seabed slope between wave gauges 7 and 12 is approximately 1:20, one-fourth the steepness of Fiskenes. The significant wave height at all wave gauges in Breivik is quite low, see Table 6.2 and Fig. 6.10, attributed mainly to the mean wave direction which leads the area to be shielded from waves without diffraction, see Fig. 6.2. What is interesting again, is that the significant wave height in simulations with directional spreading is higher at all wave gauges as shown in 6.2, likely due to waves generated at the north-east corner of the wave generation zone in a direction toward Breivik. The directional spreading of the waves ensures that not all of the wave energy at Breivik is attributed to the diffraction that occurs south of Fiskenes.

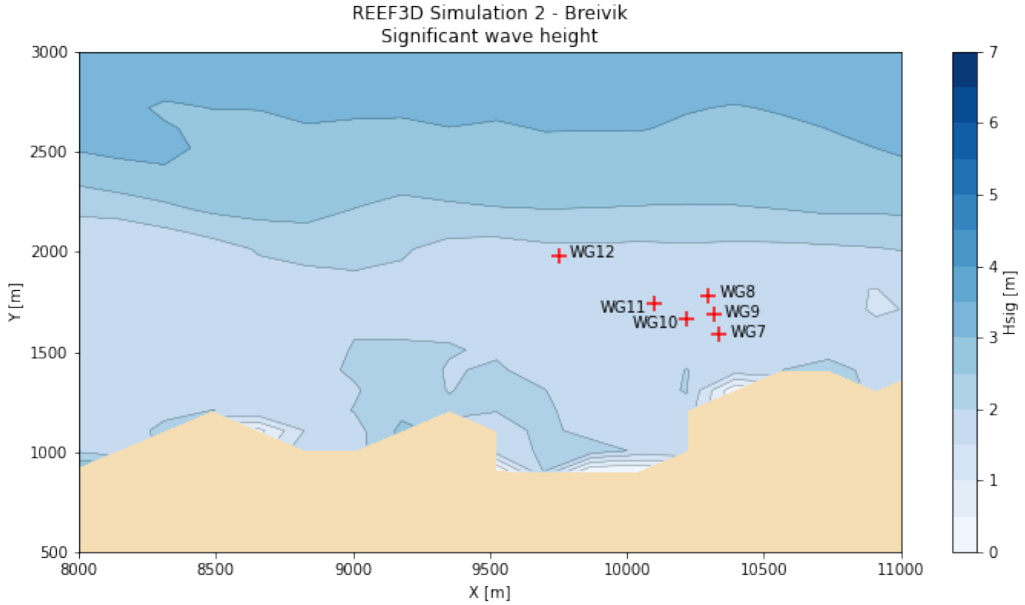

(a) H_s map Simulation 2
$\theta_{mean} = 10.7°$, $H_s = 6.67m$, $T_p = 13.7s$

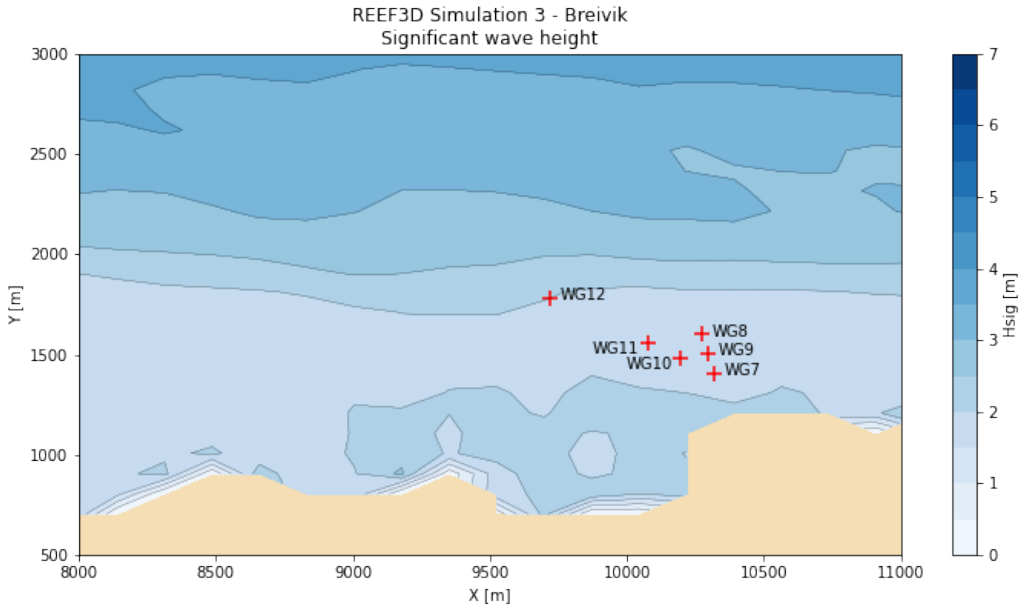

(b) H_s map Simulation 3
$\theta_{mean} = 12.8°$, $H_s = 6.41m$, $T_p = 13.7s$

Figure 6.10: H_s map from REEF3D simulations

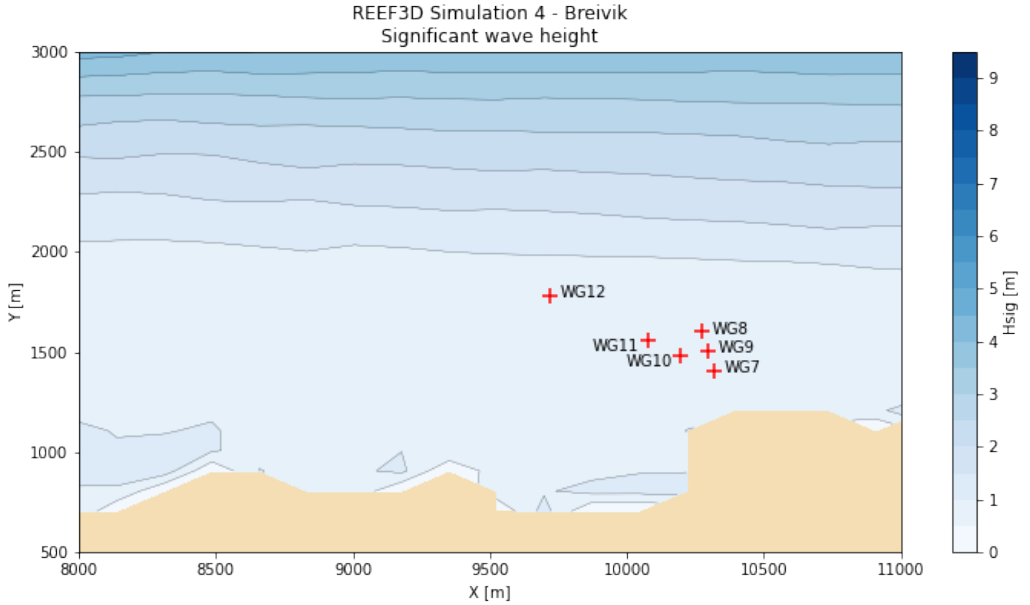

(a) H_s map Simulation 4
$\theta = 12.8°$, $H_s = 6.41m$, $T_p = 13.7s$

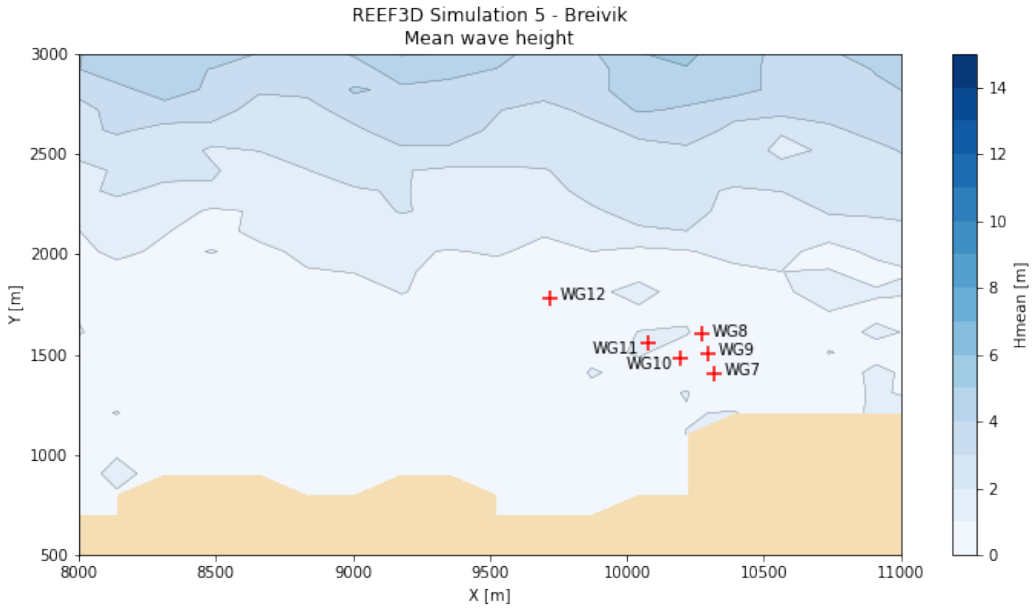

(b) H_s map Simulation 5
$\theta = 12.8°$, $H = 6.41m$, $T_p = 13.7s$

Figure 6.11: H_s and H_{mean} map from REEF3D simulations

Numerical model	STWAVE			SWAN		
Wave parameters	H_s	T_p	θ_{mean}	H_s	T_p	θ_{mean}
Offshore direction 0	7.55 m	14.3 s	5°	6.71 m	13.7 s	7.1°
Offshore direction 30	8.55 m	14.3 s	20°	6.41 m	13.7s	12.8°

Table 6.3: Comparison of key wave parameters from simulation cases in the spectral models STWAVE and SWAN

6.3 Comparison with the consulting firm

The wave modeling strategy of the consulting firm and this thesis is quite similar. A two-stage met-ocean analysis is conducted in a phase-averaged spectral model (STWAVE) in order to generate inputs for a phase-resolved model for the near-shore analysis (CGWAVE). Although the wave inputs were identical for the first simulation step in the spectral models, the results from the met-ocean study differ, as seen in Table 6.3.

Some key differences between the met-ocean analysis conducted by the consulting firm in STWAVE and the SWAN simulation conducted in this thesis, is the coupling between simulation step 1 and 2. The consulting firm decided to use one wave gauge near the edge of simulation step 2 to represent the input spectrum for simulation step 2, whereas in the SWAN simulation, a nested approach with a continuously variable spectrum was employed. Surely, different results from the met-ocean wave analysis will impact the near-shore analysis conducted in CGWAVE and REEF3D::FNPF respectively.

As seen in previous sections, REEF3D::FNPF has provided a detailed representation of various wave transformation phenomena. However, the results are not comparable to the phase-resolving results provided by the industry partner due to uncertainties of wave inputs and wave breaking treatments. Limited by the time frame of the thesis, the thorough comparison between the phase-resolving models is not performed but recommended for future work with further discussion with the industry partner.

Chapter 7

Conclusions and suggestions for further work

7.1 Summary

This master thesis has employed a combined modeling approach using two open-source models for estimating wave conditions at two proposed on-shore aquaculture facilities at Fiskenes and Breivik. The combined approach using the phase-averaging model SWAN and the phase-resolving model REEF3D::FNPF has proven to be successful. Interpolating the SWAN simulations has given more information of the met-ocean conditions at a low computational cost with acceptable accuracy. In the REEF3D::FNPF simulations, the significant wave height at the proposed locations of the breakwaters is estimated to be 2.90 meters for Fiskenes and 1.74 meters for Breivik for 200 year return period offshore swell event. It is also discovered that small changes in the location of the numerical wave gauges in the phase-resolved simulations give large variations of the significant wave height, with a wave gauge only 700 meters north-east of Fiskenes resulting in a significant wave height of 4.46 meters.

7.2 Conclusions

The combined numerical approach of the phase-averaging wave model SWAN and the phase-resolved model REEF3D::FNPF is seen to be an effective solution of coastal wave modeling, combining computational efficiency and additional information only obtainable by phase-resolved models. The model choices are also seen to be reliable, SWAN produce similar results to STWAVE for identical wave inputs, and the interpolation scheme used in the post-processing of the SWAN analysis has shown to provide reliable results for significant wave height and peak period. REEF3D::FNPF provides an efficient solution for phase-resolved wave modeling and captures wave

transformations such as diffraction, shoaling, and energy dissipation from breaking well. Both candidate locations, Breivik and Fiskenes have strong wave transformations, and Breivik has shown to have smaller waves due to more significant diffraction of waves propagating from the north.

7.3 Suggestions for further work

The study has provided many insights on wave propagation near the coast and also inspired many interesting topics for future investigations, suggested future works are summarized as the following:

- Multiple boundary wave generation in REEF3D
- Directional wave spectrum input to REEF3D
- Variable wave generation in the wave generation zone of REEF3D
- Research into directional discrete Fourier transform (DFT) on numerical wave gauges
- Refinement of directional spreading in the wave generation zone

Bibliography

N. Ahmad, A. Kamath, and H. Bihs. 3D numerical modelling of scour around a jacket structure with dynamic free surface capturing. *Ocean Engineering*, 200:107104, 3 2020. ISSN 00298018. doi: 10.1016/j.oceaneng.2020.107104.

M. Alagan Chella, H. Bihs, and D. Myrhaug. Wave impact pressure and kinematics due to breaking wave impingement on a monopile. *Journal of Fluids and Structures*, 86:94–123, 4 2019. ISSN 10958622. doi: 10.1016/j.jfluidstructs.2019.01.016.

Andfjord Salmon. Andfjord Salmon, 2021. URL https://www.andfjord.no/.

F. Ardhuin and A. Roland. The development of spectral wave models: Coastal and coupled aspects. In *Proceedings of Coastal Dynamics 2013: 7th International Conference on Coastal Dynamics*, 6 2013.

A. Baquet, J. Kim, and Z. Huang. Numerical modeling using CFD and potential wave theory for three-hour nonlinear irregular wave simulations. In *Proceedings of the International Conference on Offshore Mechanics and Arctic Engineering - OMAE*, volume 1. American Society of Mechanical Engineers (ASME), 9 2017. ISBN 9780791857632. doi: 10.1115/OMAE2017-61090. URL http://asmedigitalcollection.asme.org/OMAE/proceedings-pdf/OMAE2017/57632/V001T01A002/2532173/v001t01a002-omae2017-61090.pdf.

S. Beji and J. A. Battjes. Experimental investigation of wave propagation over a bar. *Coastal Engineering*, 19(1-2):151–162, 2 1993. ISSN 03783839. doi: 10.1016/0378-3839(93)90022-Z.

H. Bihs, A. Kamath, M. Alagan Chella, A. Aggarwal, and A. Arntsen. A new level set numerical wave tank with improved density interpolation for complex wave hydrodynamics. *Computers and Fluids*, 140:191–208, 11 2016. ISSN 00457930. doi: 10.1016/j.compfluid.2016.09.012.

H. Bihs, W. Wang, C. Pakozdi, and A. Kamath. REEF3D::FNPF—A Flexible Fully Nonlinear Potential Flow Solver. *Journal of Offshore Mechanics and Arctic Engineering*, 142(4), 8 2020. ISSN 0892-7219. doi: 10.1115/1.4045915.

N. Booij, R. C. Ris, and L. H. Holthuijsen. A third-generation wave model for coastal regions 1. Model description and validation. *Journal of Geophysical Research: Oceans*, 104(C4):7649–7666, 4 1999. ISSN 21699291. doi: 10.1029/98JC02622. URL https://agupubs.onlinelibrary.wiley.com/doi/full/10.1029/98JC02622https://agupubs.onlinelibrary.wiley.com/doi/abs/10.1029/98JC02622https://agupubs.onlinelibrary.wiley.com/doi/10.1029/98JC02622.

EMODnet. EMODnet Bathymetry, 2021. URL https://www.emodnet-bathymetry.eu/.

T. Fjørtoft and T. Fondevik. Land-based salmon farming in Norway – laws and regulations, 2020. URL https://salmonbusiness.com/land-based-salmon-farming-in-norway-laws-and-regulations/.

GDAL. GDAL — GDAL documentation, 2021. URL https://gdal.org/.

N. G. Jacobsen, D. R. Fuhrman, and J. Fredsøe. A wave generation toolbox for the open-source CFD library: OpenFoam®. *International Journal for Numerical Methods in Fluids*, 70(9):1073–1088, 11 2012. ISSN 02712091. doi: 10.1002/fld.2726. URL https://onlinelibrary.wiley.com/doi/full/10.1002/fld.2726https://onlinelibrary.wiley.com/doi/abs/10.1002/fld.2726https://onlinelibrary.wiley.com/doi/10.1002/fld.2726.

J. H. Jensen, E. Madsen, and J. Fredsøe. oblique flow over dredged channels. II: Sediment transport and
} morphology. *Journal of Hydraulic Engineering (Reston)*, 125(11):1190–1198, 1999. ISSN 0733-9429. URL https://orbit.dtu.dk/en/publications/oblique-flow-over-dredged-channels-ii-sediment-transport-and-morp.

G. S. Jiang and C. W. Shu. Efficient implementation of weighted ENO schemes. *Journal of Computational Physics*, 126(1):202–228, 6 1996. ISSN 00219991. doi: 10.1006/jcph.1996.0130.

Kartverket. Kartverket, 2021a. URL https://dybdedata.kartverket.no/DybdedataInnsyn/.

Kartverket. Kartverket, 2021b. URL https://hoydedata.no/LaserInnsyn/.

T. Martin, A. Kamath, and H. Bihs. A Lagrangian approach for the coupled simulation of fixed net structures in a Eulerian fluid model. *Journal of Fluids and Structures*, 94:102962, 4 2020. ISSN 10958622. doi: 10.1016/j.jfluidstructs.2020.102962.

Norwegian Building Authority. Regulations om technical requirements for construction works (TEK17). Technical report, 2017.

S. Osher and J. A. Sethian. Fronts propagating with curvature-dependent speed: Algorithms based on Hamilton-Jacobi formulations. *Journal of Computational Physics*, 79(1):12–49, 11 1988. ISSN 10902716. doi: 10.1016/0021-9991(88)90002-2.

D. Pollock. Smoothing with Cubic Splines. In *Handbook of Time Series Analysis, Signal Processing, and Dynamics*, pages 293–322. Elsevier, 1999. doi: 10.1016/b978-012560990-6/50013-0.

M. Reistad, Breivik, H. Haakenstad, O. J. Aarnes, and B. R. Furevik. A high-resolution hindcast of wind and waves for The North Sea, The Norwegian Sea and The Barents Sea Title A high-resolution hindcast of wind and waves for The North Sea, The Norwegian Sea and The Barents Sea. 2009. ISSN 1503-8025.

C. W. Shu and S. Osher. Efficient implementation of essentially non-oscillatory shock-capturing schemes. *Journal of Computational Physics*, 77(2):439–471, 8 1988. ISSN 10902716. doi: 10.1016/0021-9991(88)90177-5.

P. Smit, M. Zijlema, and G. Stelling. Depth-induced wave breaking in a non-hydrostatic, near-shore wave model. *Coastal Engineering*, 76:1–16, 6 2013. ISSN 03783839. doi: 10.1016/j.coastaleng.2013.01.008.

M. Sussman. A level set approach for computing solutions to incompressible two-phase flow. *Journal of Computational Physics*, 114(1):146–159, 9 1994. ISSN 00219991. doi: 10.1006/jcph.1994.1155.

SWAN. SWAN, 2020. URL https://www.tudelft.nl/en/ceg/about-faculty/departments/hydraulic-engineering/sections/environmental-fluid-mechanics/research/swan/.

H. A. van der Vorst. Bi-CGSTAB: A Fast and Smoothly Converging Variant of Bi-CG for the Solution of Nonsymmetric Linear Systems. *SIAM Journal on Scientific and Statistical Computing*, 13(2):631–644, 3 1992. ISSN 0196-5204. doi: 10.1137/0913035. URL https://epubs.siam.org/page/terms.

W. Wang. Large-Scale Phase-Resolved Wave Modelling for the Norwegian Coast. 2020.

W. Wang, A. Kamath, C. Pakozdi, and H. Bihs. Investigation of focusing wave properties in a numericalwave tank with a fully nonlinear potential flow model. *Journal of Marine Science and Engineering*, 7(10), 10 2019. ISSN 20771312. doi: 10.3390/jmse7100375.

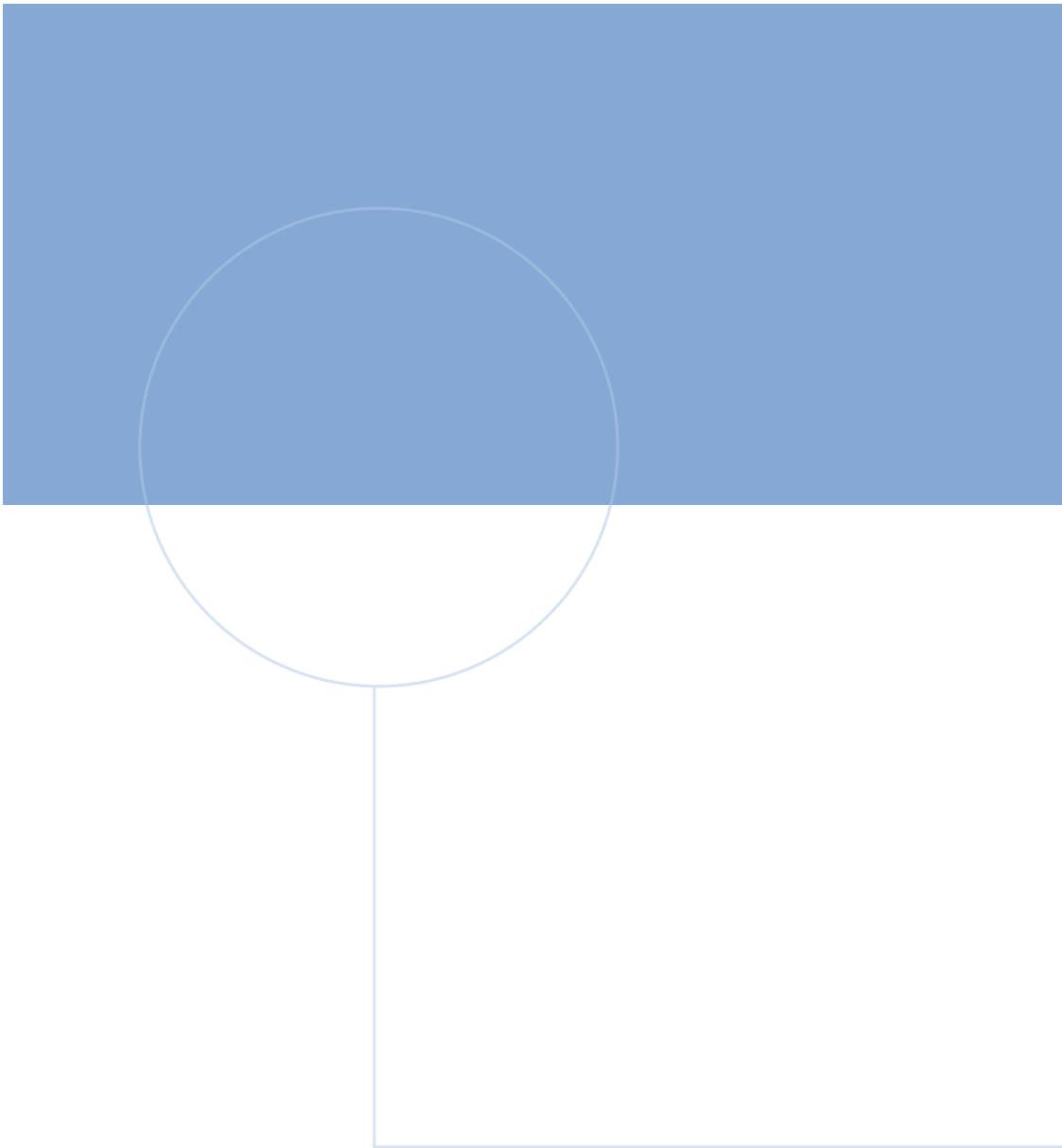

NTNU

Kunnskap for en bedre verden